



Peer review status:

This is a non-peer-reviewed preprint submitted to EarthArXiv
and is currently under review at *Geophysical Journal
International*.


THEORETICAL BACKGROUND FOR FULL-WAVEFORM INVERSION WITH DISTRIBUTED ACOUSTIC SENSING AND INTEGRATED STRAIN SENSING


A NON-PEER REVIEWED PREPRINT

 **Sebastian Noe***
Institute of Geophysics
ETH Zurich
Zurich, Switzerland
sebastian.noe@eaps.ethz.ch

 **Katinka Tuinstra**
Swiss Seismological Service
ETH Zurich
Zurich, Switzerland
katinka.tuinstra@sed.ethz.ch

 **Sara Klaasen**
Institute of Geophysics
ETH Zurich
Zurich, Switzerland
sara.klaasen@eaps.ethz.ch

 **Lion Krischer**
Mondaic AG
Zurich, Switzerland
lion.krischer@mondaic.ch

 **Andreas Fichtner**
Institute of Geophysics
ETH Zurich
Zurich, Switzerland
andreas.fichtner@eaps.ethz.ch

ABSTRACT

Full-waveform inversion (FWI) is a powerful imaging technique that produces high-resolution subsurface models. In seismology, FWI workflows are traditionally based on seismometer recordings. The development of fibre-optic sensing presents opportunities for harnessing information from new types of measurements. With dense spatial and temporal sampling, fibre-optic sensing captures the seismic wavefield at metre-scale resolution along the cable. Applying FWI to fibre-optic measurements requires the reformulation of the forward and adjoint problems due to two fundamental differences to seismometer data: i) fibre-optic measurements are sensitive to strain rather than translational motion, and ii) they do not represent the motion at a single spatial point, but instead capture the average deformation over a pre-defined cable segment, known as the gauge length. This study introduces the theoretical and computational framework to apply FWI to distributed acoustic sensing (DAS) and integrated fibre-optic sensing (IFOS) in 3-D for complex cable geometries and subsurface structures. Our proposed forward model for fibre-optic data incorporates gauge length effects, and direction— and curvature-dependent sensitivity, as well as arbitrary cable layouts. For the numerical simulations, we use a spectral-element solver that allows us to incorporate surface topography, and coupled viscoacoustic and viscoelastic rheologies. We derive an adjoint source based on moment tensors. In illustrative examples, we present how our theoretical developments can be used in inversions of synthetic fibre-optic data generated for a realistically curved cable placed on irregular topography. As examples, we invert for source parameters, including moment tensor, location, and origin time for noise-free DAS data, noise-contaminated DAS data, and IFOS data. Further, we present FWI for the three data groups to obtain 3-D tomographic images of P- and S-wave speeds. In all example inversion, we compare how close the found model is to the ground truth. The codes to produce these results are accessible and ready to be applied to real data inversions.

Keywords Inverse theory · Computational seismology · Distributed acoustic sensing · Seismic tomography · Waveform inversion

*Corresponding author

1 Introduction

Seismic data acquisition through fibre-optic sensing has revolutionised the field of seismology by increasing the total volume and spatial density of data while often re-purposing pre-existing infrastructure. Distributed acoustic sensing (DAS) samples the deformation along a fibre with high temporal and spatial resolution through the back-scattering of laser pulses sent into the fibre. Beyond the ability of DAS to detect and measure earthquakes (Li & Zhan, 2018; Yu et al., 2019), its flexibility in deployments has turned DAS into a valuable monitoring tool in a variety of environments, including volcanoes (Nishimura et al., 2021; Klaasen et al., 2021; Currenti et al., 2021; Jousset et al., 2022), glaciers (Walter et al., 2020; Hudson et al., 2021; Fichtner et al., 2023), landslides (Ouellet et al., 2024; Kang et al., 2024), avalanches (Paitz et al., 2023) and urban areas (Fang et al., 2020; Azzola et al., 2023; Ehsaninezhad et al., 2024; Smolinski et al., 2024).

An alternative interrogation method of fibre-optic cables, named integrated fibre-optic sensing (IFOS), has emerged over the past years. It measures deformation-induced phase changes of the transmitted laser signal through the fibre instead of the back-scattered light pulses. With this method, the entire fibre length produces a single measurement channel. Compared to DAS, the feasible interrogation range significantly increases from ~ 100 km to thousands of km. Such a system can be interpreted as summing over all DAS-channels along the fibre to produce a single data trace (Bowden et al., 2022). Because of the spatial extent of the sensitivity of IFOS data along the cable, it is more challenging to interpret the waveforms (Fichtner et al., 2022b). Nevertheless, IFOS can be cost-efficient to install (Bogris et al., 2022), or obtained through systems whose primary goal is not seismic data acquisition such as metrological networks (Marra et al., 2018; Noe et al., 2023; Donadello et al., 2024), or through infrastructure owned by internet providers (Zhan et al., 2021; Marra et al., 2022).

Given that fibre-optic cables capture the full seismic wavefield, though only in one dimension, full-waveform inversion (FWI) appears well suited to analysing DAS and IFOS measurements to characterise both the propagation medium and the wavefield sources. With an iterative optimisation scheme based on the adjoint method (Tarantola, 1984; Fichtner et al., 2006; Liu & Tromp, 2006), FWI accounts for the non-linear relationship of model parameters and the recorded wavefield. Moreover, the numerical model can be tuned to mirror the physical complexity of seismic data by incorporating topography, bodies of water, and nearly arbitrary 3-D subsurface heterogeneities; all effects influencing wavefield propagation, and, by extension, fibre-optic measurements (Igel et al., 2024). Through the exploitation of complete seismic recordings, FWI can achieve a higher resolution than, for example, methods based on the ray approximation of few selected seismic phases (e.g. Tromp, 2020; Schouten et al., 2024). Tomography with FWI has been applied across various scales, from small-scale exploration settings on the order of hundreds of metres (Virieux & Operto, 2009; Borisov et al., 2020; Berti et al., 2024), to regional scales of hundreds of kilometres (e.g. Rodgers et al., 2024; Liu et al., 2024), to global scales (e.g. Lekić & Romanowicz, 2011; Lei et al., 2020; Thrastarson et al., 2024). In turn, improved 3-D wave speed models benefit the accuracy of earthquake source characterisation (Simutė et al., 2023; Doody et al., 2025).

While detection and monitoring with DAS have evolved into well-established techniques, the potential for seismic imaging has not yet been fully realised. Even though the computation of dispersion curves with DAS data (Luo et al., 2021b; Lior et al., 2022; Spica et al., 2022; Smolinski et al., 2024) and traveltime analysis (Lellouch et al., 2019; Piana Agostinetti et al., 2022; Abukrat et al., 2023; Biondi et al., 2023, e.g.) have shown promising results for imaging, the full formulation of how to derive a 3-D subsurface model based on FWI is yet to be achieved. A challenge with inversions using DAS is the potentially variable orientation of the cable over its entire length that changes the sensitivity to body and surface wave arrivals. Therefore, successful FWI imaging applications with DAS have been limited to near-straight borehole fibre-optic cables only (Eaid et al., 2023; Yust et al., 2023; Qu et al., 2024). For event-based imaging techniques, sufficient knowledge of the source characteristics is important; however, source inversions with DAS data suffer from many of the same challenges. Studies have shown that polarity patterns in the near-field strain recorded with DAS can be used to constrain focal planes (Vera Rodriguez & Wuestefeld, 2020; Luo et al., 2021a). Other approaches to deriving the radiation pattern include f - k analysis (e.g. Lentas et al., 2023) and correlated wavefields (e.g. Nishimura et al., 2021; Li et al., 2023). Moreover, the location of sources can be inferred from picked travel times of seismic phases (Piana Agostinetti et al., 2022; Klaasen et al., 2023; Yin et al., 2023; Tuinstra et al., 2024; Katakami et al., 2025).

However, several challenges are posed when extending established FWI workflows (e.g. Modrak et al., 2018; Rodgers et al., 2024; Thrastarson et al., 2024) to fibre-optic data: i) The orientation of the cable introduces differential angular sensitivity to all wave phases. ii) Fibre-optic sensing records the strain of the medium instead of translational motion, such as velocity or acceleration. iii) Fibre-optic measurements are not point measurements but instead an average of the strain over a cable segment, an effect especially apparent in the presence of cable curvature or when the seismic wavelengths are comparable to the gauge length. All of these challenges must be addressed to leverage fibre-optic data for quantitative seismology.

The goal of this study is to provide the theoretical background for FWI with fibre-optic data. We show how to formulate the adjoint sources for the inverse problem, where we demonstrate that the theoretical findings of Fichtner et al. (2022b) implicitly hold in the first-order approximation. We apply the adjoint sources to inverse problems with synthetic data, where we solve for earthquake source parameters and the wave speed model using both DAS and IFOS.

2 Theory

FWI aims to match the numerically computed response at seismic receivers to observations by adjusting the underlying model parameters. The medium can be expressed in terms of anisotropic P- and S-wave speeds, material density and attenuation, while the seismic source may be designed with arbitrary complexity, for example, as a point source or a finite fault. Typically, however, only a subset of these model parameters is included in the data fitting process. Attenuation and density are often fixed, and source models are reduced to a moment tensor point source in space and time. Furthermore, for simplicity or thanks to sufficient prior knowledge, inversion workflows often address either structural parameters or source parameters in their approach.

The adjoint method is a common choice to efficiently derive the gradient of an objective function with respect to the underlying model parameters in FWI problems (e.g. Lailly, 1983; Tarantola, 1984; Liu & Tromp, 2006; Fichtner et al., 2006). It requires the numerical solution of the seismic wave equation subject to a seismic source, and the solution to a complementary wave equation, the adjoint problem. In the adjoint problem, the receivers emit seismic energy with a source-time function based on the misfit between the forward model and the observations. The scalar product of the forward and adjoint fields yields the model gradient for structural parameters, meaning that for a gradient computation, the total number of simulations equals twice the number of considered forward sources. In contrast, the earthquake source gradient can be derived directly from the adjoint wavefield (e.g. Liu et al., 2004; Tromp et al., 2005; Kim et al., 2011). Due to the non-linear relationship of the wavefield to the subsurface properties, as well as the source location and time, the model must be refined over several iterations, with a new gradient computed at each step.

In the following, we develop the complete theoretical framework for forward and adjoint problems in FWI for fibre-optic sensing, accounting for the directionality of sensitivity, gauge lengths, and the measurement unit of strain.

2.1 The forward problem

Our forward model builds on Fichtner et al. (2022b), where the general relationship between the deformation tensor \mathbf{F} and the phase delay of a laser pulse ϕ along one channel is given by

$$\phi(t) \propto \int_{-\frac{l}{2}}^{\frac{l}{2}} |(\mathbf{I} + \mathbf{F}(s, t))\mathbf{e}(s)| ds, \quad (1)$$

where l is the gauge length, \mathbf{I} is the identity matrix, t is time, and \mathbf{e} is the local unit tangent vector at arc length s along the fibre in 3-D space. The proportionality absorbs terms related to the laser wavelength and the photoelastic effect. Equation (1) is generally valid and describes the non-linear relationship between the measurements and the deformation. In seismology, deformations of interest are generally small ($\mathbf{F} \ll \mathbf{I}$), leading to the linearised form of eq. (1),

$$\phi(t) \propto \int_{-\frac{l}{2}}^{\frac{l}{2}} \mathbf{e}^T(s) \boldsymbol{\epsilon}(s, t) \mathbf{e}(s) ds, \quad (2)$$

where $\boldsymbol{\epsilon} = \frac{1}{2}(\mathbf{F} + \mathbf{F}^T)$ denotes the strain tensor (Fichtner et al., 2022b). DAS interrogators scale the phase delay measurements to convert them to strain, allowing us to drop the proportionality in eq. 2. Thus, we arrive at the general equation for DAS measurements (e.g. Martin et al., 2021; Kennett, 2024):

$$\bar{\epsilon}_{\text{DAS}}(s_c, t) = \frac{1}{l} \int_{s_c - \frac{l}{2}}^{s_c + \frac{l}{2}} \mathbf{e}^T(s) \boldsymbol{\epsilon}(s, t) \mathbf{e}(s) ds. \quad (3)$$

Equation (3) is evaluated at the channel location at the centre of the gauge length, s_c , along the interrogated cable. The bar on $\bar{\epsilon}$ indicates averaging of strain over a cable segment in contrast to the local strain tensor $\boldsymbol{\epsilon}$.

The gauge length l in DAS systems is generally set before data collection begins and often varies between 1 and 10 m. As shown by Bowden et al. (2022), the measurements from DAS systems can be linked to phase-transmission techniques by integrating along all channels. This effectively results in gauge lengths corresponding to the entire length of the cable, $l = l_{\text{fibre}}$, and evaluating the strain field only at $s_c = \frac{l_{\text{fibre}}}{2}$.

$$\bar{\epsilon}_{\text{IFOS}}(t) = \frac{1}{l_{\text{fibre}}} \int_0^{l_{\text{fibre}}} \mathbf{e}^T(s) \boldsymbol{\epsilon}(s, t) \mathbf{e}(s) ds. \quad (4)$$

Numerically, the integral in eq. (3) can only be evaluated at a finite number of points per gauge length (N_g)

$$\bar{\epsilon}(s_c, t) \approx \frac{1}{l} \sum_{g=0}^{N_g} \mathbf{e}^T(s_{c,g}) \boldsymbol{\epsilon}(s_{c,g}, t) \mathbf{e}(s_{c,g}) \Delta s \quad (5)$$

$$= \frac{1}{N_g} \sum_{g=0}^{N_g} \mathbf{e}^T(s_{c,g}) \boldsymbol{\epsilon}(s_{c,g}, t) \mathbf{e}(s_{c,g}), \quad (6)$$

where the index g defines evaluation points with a spacing of $\Delta s = \frac{l}{N_g}$ along the gauge length for a channel centred at location s_c . Hence, the discretisation points $s_{c,g}$ are located at

$$s_{c,g} = s_c + l \left(\frac{g}{N_g} - \frac{1}{2} \right). \quad (7)$$

The solution to the forward problem in eq. (6) can be implemented in all numerical wave propagation solvers. If the strain field is not provided as an output of the solver, it can be derived explicitly as the spatial derivative from the displacement vector field \mathbf{u} using, for example, a finite-difference stencil. Furthermore, the evaluation points $s_{c,g}$ along the fibre do not need to coincide with the 3-D simulation grid, requiring an interpolation of the strain field to obtain the values at the evaluation points $\boldsymbol{\epsilon}(s_{c,g}, t)$. Depending on the simulated wavelength and the gauge length, N_g can be appropriately chosen to ensure sufficient sampling of the strain field $\boldsymbol{\epsilon}$.

2.2 The adjoint problem

Given that we solved the forward problem of how to compute synthetic fibre-optic data with eq. (6), we will now focus on the adjoint formulation. First, we inspect the physical system at hand. The seismic wave equation operator \mathbf{L} connects the seismic displacement field $\mathbf{u} = \mathbf{u}(\mathbf{x}, t)$ through medium parameters \mathbf{m}_v to a source term \mathbf{f} that depends on source parameters \mathbf{m}_s ,

$$\mathbf{L}(\mathbf{u}; \mathbf{m}_v, \mathbf{x}, t) = \mathbf{f}(\mathbf{m}_s; \mathbf{x}, t). \quad (8)$$

The objective function is evaluated for N_c channels at locations s_c along the fibre. A general objective function reads as follows

$$\chi = \frac{1}{N_c} \int_{t_0}^{t_1} \int_{\Omega} h(\bar{\epsilon}(\mathbf{u}(\mathbf{x}, t)) \delta(\mathbf{x} - \mathbf{x}_c) d\Omega dt, \quad (9)$$

where the misfit kernel h quantifies the match between observed and computed traces at the central channel location \mathbf{x}_c situated at arc length s_c in the 3-D spatial domain Ω . A common choice for h is the squared difference $h(\bar{\epsilon}) = \frac{1}{2}(\bar{\epsilon} - \bar{\epsilon}_{\text{obs}})^2$.

The adjoint equation for computing a model gradient of the objective function χ is (e.g. Fichtner et al., 2006; Liu & Tromp, 2006)

$$\mathbf{L}^\dagger(\mathbf{u}^\dagger; \mathbf{m}_v, \mathbf{x}, t) = -\frac{\partial h}{\partial \mathbf{u}} \delta(\mathbf{x} - \mathbf{x}_c) \quad (10)$$

with the adjoint operator \mathbf{L}^\dagger acting on the adjoint wavefield \mathbf{u}^\dagger and a source term given by the misfit kernel h . Equation (10) holds for both the medium properties (\mathbf{m}_v) and the source parameters (\mathbf{m}_s) and is independent of the measurement unit of the observations (see derivation in appendix A). Therefore, we must derive the source term in eq. (10) to solve the adjoint problem.

As the full adjoint source term is the sum of individual channel contributions, we limit the following derivations to the source contribution of a single channel, based on its kernel evaluation h_c . Moreover, we introduce index notation with $k = [1, 2, 3]$. Expanding the source term of eq. (10) using the forward relationship of eq. (6) leads to

$$f_{c,k}^\dagger = -\frac{\partial h_c}{\partial u_k} \quad (11)$$

$$= -\frac{\partial h_c}{\partial \bar{\epsilon}} \frac{\partial \bar{\epsilon}}{\partial u_k} \quad (12)$$

$$\approx -\frac{\partial h_c}{\partial \bar{\epsilon}} \frac{\partial}{\partial u_k} \frac{1}{N_g} \sum_{g=0}^{N_g} e(\mathbf{x}_{c,g})^T \boldsymbol{\epsilon}(\mathbf{x}_{c,g}) e(\mathbf{x}_{c,g}) \quad (13)$$

$$= -\frac{1}{N_g} \sum_{g=0}^{N_g} \frac{\partial h_c}{\partial \bar{\epsilon}} \mathbf{e} \mathbf{e}^T : \frac{\partial \boldsymbol{\epsilon}}{\partial u_k} \quad (14)$$

$$= -\frac{1}{N_g} \sum_{g=0}^{N_g} \frac{\partial h_c}{\partial \bar{\epsilon}} \mathbf{e} \mathbf{e}^T : \hat{\mathbf{x}}_k^T \frac{\partial \boldsymbol{\epsilon}}{\partial \mathbf{u}}, \quad (15)$$

where $\hat{\mathbf{x}}_k$ identifies the k^{th} unit base vector and $\mathbf{A} : \mathbf{B} = A_{ij} B_{ij}$ is the matrix scalar product with Einstein summation convention. In eq. (15), we find the partial derivative of the strain field with respect to the displacement wavefield $\frac{\partial \boldsymbol{\epsilon}(\mathbf{u})}{\partial \mathbf{u}}$. This derivative can be evaluated using a scalar product – defined in the spatial domain Ω – with an infinitesimally small perturbation in the wavefield $\delta \mathbf{u}$, leading to

$$\int_{\Omega} f_{c,k}^\dagger \cdot \delta \mathbf{u} d\Omega = \int_{\Omega} -\frac{1}{N_g} \sum_{g=0}^{N_g} \hat{\mathbf{x}}_k \frac{\partial h_c}{\partial \bar{\epsilon}} \mathbf{e} \mathbf{e}^T(\mathbf{x}_{c,g}) : \left(\frac{\partial \boldsymbol{\epsilon}(\mathbf{u})}{\partial \mathbf{u}} \delta \mathbf{u} \right) d\Omega \quad (16)$$

$$= \int_{\Omega} -\frac{1}{N_g} \sum_{g=0}^{N_g} \hat{\mathbf{x}}_k \frac{\partial h_c}{\partial \bar{\epsilon}} \mathbf{e} \mathbf{e}^T(\mathbf{x}_{c,g}) : \left(\boldsymbol{\epsilon}(\mathbf{u} + \delta \mathbf{u}) - \boldsymbol{\epsilon}(\mathbf{u}) \right) d\Omega \quad (17)$$

$$= -\frac{1}{N_g} \sum_{g=0}^{N_g} \int_{\Omega} \hat{\mathbf{x}}_k \delta(\mathbf{x} - \mathbf{x}_{c,g}) \frac{\partial h_c}{\partial \bar{\epsilon}} \mathbf{e} \mathbf{e}^T(\mathbf{x}) : \boldsymbol{\epsilon}(\delta \mathbf{u}) d\Omega. \quad (18)$$

To arrive at eq. (18), we use the linearity of the strain operator $\boldsymbol{\epsilon}(\mathbf{u})$ and introduce delta-functions at the discretisation points $\mathbf{x}_{c,g}$ of the gauge length to move the integral inside the sum. In eq. (18), we find a sum of moment tensor sources in the weak formulation of the wave equation (e.g. Faccioli et al., 1997; Komatitsch & Vilotte, 1998), formulated as

$$\int_{\Omega} f_k(\mathbf{x}_s, t) \cdot \mathbf{w} d\Omega = \int_{\Omega} \hat{\mathbf{x}}_k \delta(\mathbf{x} - \mathbf{x}_s) S(t) \mathbf{M} : \boldsymbol{\epsilon}(\mathbf{w}) d\Omega, \quad (19)$$

where sources are initialized at locations \mathbf{x}_s . In the spectral-element method, the test function $\mathbf{w}(\mathbf{x})$ is approximated by a product of Lagrange polynomials (e.g. Faccioli et al., 1997; Komatitsch & Vilotte, 1998). Comparing eqs. (18) and (19), we identify the symmetric moment tensor given by the local orientation of the cable

$$\mathbf{M} = \mathbf{e} \mathbf{e}^T, \quad (20)$$

and the source-time function depending on the misfit kernel h

$$S(t) = -\frac{\partial h_c}{\partial \bar{\epsilon}}. \quad (21)$$

Often in fibre-optic sensing, traces are analysed as strain rates rather than absolute strains. In the case where the misfit kernel evaluates strain rates (i.e. $h = h(\dot{\bar{\epsilon}})$), the source-time function of the adjoint source term changes to

$$S(t) = \frac{\partial}{\partial t} \frac{\partial h_c}{\partial \dot{\bar{\epsilon}}}. \quad (22)$$

The sign change in eq. (22) arises from the adjoint of a first derivative (appendix B). This is the form of the source term that will be used throughout the results of this study.

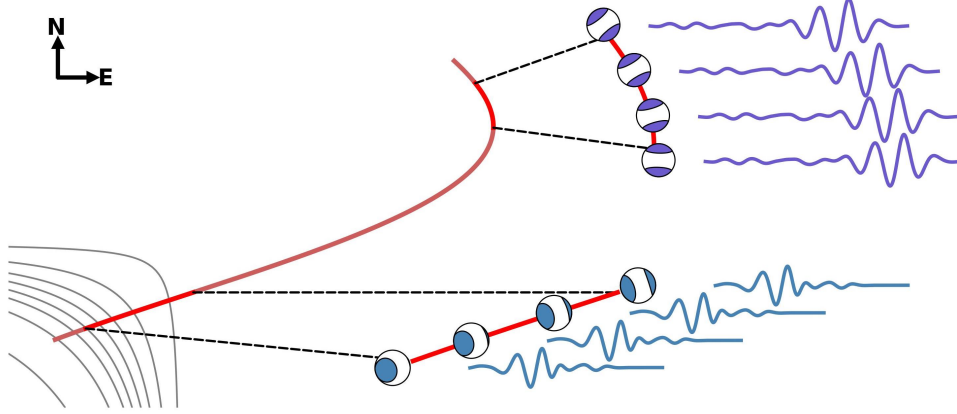


Figure 1: Schematic illustration of the adjoint source for strain measurements on a fibre-optic cable, with focus on two channels with a gauge length discretisation $N_g = 4$. In the numerical implementation of the adjoint source, there are N_g moment tensors sharing the same source-time function. The southwestern channel follows an increasingly steep slope indicated by the contour lines. This results in progressively upwards-rotated moment tensor sources. For an effective implementation of the adjoint source as a line source, the discretisation N_g should be chosen depending on the simulated wavelength and gauge length.

2.3 Implications of the adjoint source term

The adjoint sources for fibre-optic data, defined in eq. (20), are symmetric moment tensor point sources. This contrasts with vector sources used in the adjoint equations for seismometer data, as well as with asymmetric moment tensor sources for rotational measurements (Fichtner & Igel, 2009). The moment tensor adjoint sources are visualised in Fig. 1 for two channels of a fibre-optic cable. Within a single channel, the source-time function $\frac{\partial}{\partial t} \frac{\partial h}{\partial \epsilon}$ is shared among all discretised point sources along the cable segment for the respective channel, which we set to $N_g = 4$ here for illustrative purposes. The orientations of the moment tensors ee^T along a single gauge length vary with the fibre orientation. In the upper channel of Fig. 1, the orientation of the moment tensors changes with the curvature of the fibre within the gauge length, accounting for the variable sensitivity along the channel. The formulation of the adjoint source holds in a 3-D medium and is therefore valid for fibres in boreholes or where the fibre layout follows surface topography. The 3-D effect is visualised in the lower channel in Fig. 1, where the gauge length is along increasingly steep topography, resulting in upwards rotated moment tensor sources. The findings for the source-time function hold for any misfit kernel h used in adjoint problems.

This raises the question about an adequate discretisation for a single gauge length within the forward model (eq. 6) and the adjoint. A proper value for N_g varies with the simulated seismic wavelengths and the gauge length. For $N_g = 1$, the sensitivity is reduced to a point measurement at the centre of the gauge length, potentially introducing wrong arrival times, as seismic phases may arrive at up to half a gauge length displaced in the simulations. The discretisation $N_g = 2$ correctly models the arrival times at the start and end of the gauge length; however, it may still underrepresent the integrated strain along the segment, ignoring potential curvatures. In Fig. 2(a), such an underrepresentation for a single gauge length is visualised for $N_g = 3$. For this combination of gauge length and simulated wavelength, there is an adjoint source emitted in the centre of the gauge length, where there should not be any sensitivity (Fichtner et al., 2022b). However, when significantly increasing N_g , the lined-up moment tensors correctly represent the gauge length (Fig. 2b), where only the start and end points of the gauge length contribute to the sensitivity. If the gauge length includes curvature (Fig. 2c), the points of curvature act as additional sensitivity points and therefore contribute to the adjoint wavefield, which conforms with the theoretical sensitivity of a single channel (Fichtner et al., 2022b). Notably, curvature is not explicitly stated as a scaling factor for f^i in eq. (18), but the lined-up moment tensors forming the adjoint source correctly account for curvature regardless. Based on a different, but equivalent, linearisation of eq. (1), one may also account for curvature explicitly, which has been addressed by Fichtner et al. (2022a).

Given the adjoint source term in eq. (18), model gradients of the objective function can be computed in the same manner as in inverse problems based on seismometer data, specifically through the scalar-product of forward and adjoint displacement fields for tomographic parameters (e.g. Fichtner et al., 2006; Liu & Tromp, 2006), and by evaluating the adjoint strain field at the source location for source parameters (Tromp et al., 2005; Kim et al., 2011).

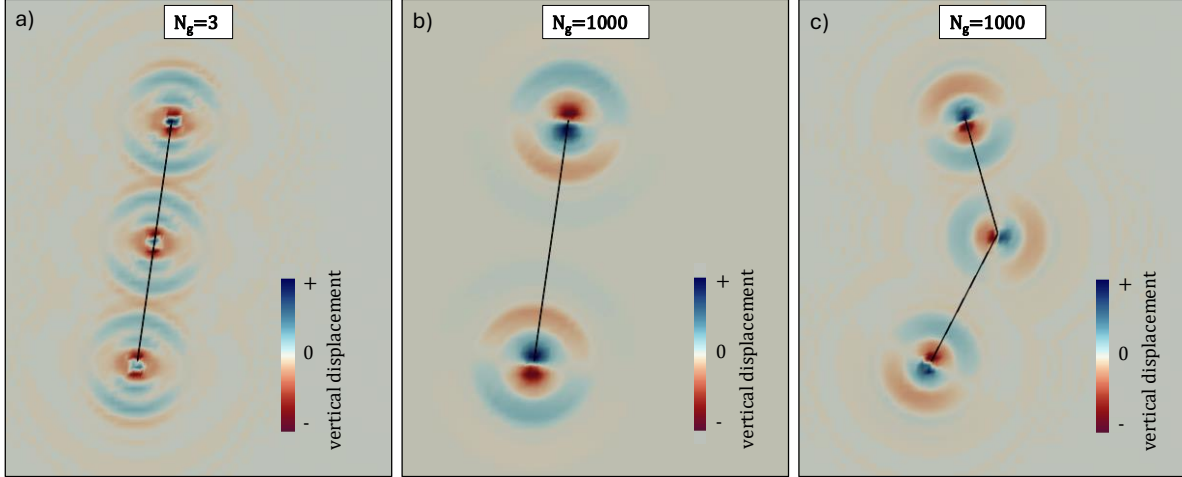


Figure 2: Snapshots of the adjoint wavefield radiating from a single channel: a) Underrepresented adjoint source along a straight channel, as seen by the central adjoint source that mistakenly acts as a point of sensitivity. b) Accurately modelled adjoint source for a straight channel, where only the start and end points of the gauge length contribute to the adjoint wavefield; c) Accurately modelled adjoint source for a channel with a kink, where, in addition to the start and end points, the segment with curvature radiates a non-compensated adjoint source.

3 Synthetic FWI

3.1 Setup and goals

In the following, we provide illustrative example inversions based on the adjoint source term for fibre-optic data in eq. (18). These inversions use synthetic data that was generated with a known model, facilitating the direct comparison between the ground truth and the inverted best-fitting model. We present standard inversion scenarios for source and structural parameters using DAS data with and without noise, as well as IFOS data. We provide successful and unsuccessful inversions with some discussion.

The design of our synthetic experiment reflects a realistic setting for environmental monitoring, such as assessing landslide stability, glacier dynamics, or volcanic activity. Therefore, a requirement of the cable is to be placed such that it follows topography. Additionally, repurposing existing fibre-optic cables for interrogation is often preferred in terms of cost and time efficiency, which imposes the constraint that the cable geometry reflects a realistic location along a hypothetical train line or a road. Furthermore, the fibre should have a mix of heavily curved and straight segments to assess the influence of changing directionality of the sensitivity. We design a test setup that meets these requirements (see Fig. 3a). The cable covers an elevation difference of roughly 360 m over its 8 km length and follows the topography from the valley to the ridge. In fact, the fibre-optic cable geometry is inspired by the shape of the train tracks of the *Uetlibergbahn* in Zurich (Switzerland) to the top of of the Albis mountain range. The subsurface structure is a layered medium (see Fig. 8).

The artificial observed data in the inversions originate from numerical simulations of 10 fictitious earthquakes within the domain. The locations of earthquake epicentres are at a maximum depth of 500 m below sea level. The earthquakes are modelled as moment tensor point sources with a filtered Heaviside function serving as the source-time function in the frequency range of 0.5–1 Hz. The DAS measurements are conducted with a gauge length of 8 m, resulting in 1000 channels over the 8 km length. The minimum wave length of 500 m is much greater than the gauge length, hence we select $N_g = 2$ to accurately simulate arrival times at the start and end of each gauge length segment. For the IFOS measurements, we increase the discretisation to $N_g = 2000$ to match the number of evaluation points in the DAS examples. Numerical simulations are performed with the spectral-element wave propagation solver *Salvus* (Afanasyev et al., 2019), which enables implementation of absorbing boundaries, the free surface, topography, and moment tensor point sources for both forward and adjoint wavefield computations. We show the artificial data for events used for the source inversions in Fig. 3(b). In the examples including noise, the recordings have a maximal signal-to-noise ratio (SNR) of 10, where the noise field is correlated for neighbouring channels over a distance of 500 m along the fibre (see Fig. 3b). The software package *Pyber*, developed for this study, interacts with the wave propagation solver, reads out the strain data from synthetic wavefields, computes the adjoint source term, and overall automates the FWI workflow.

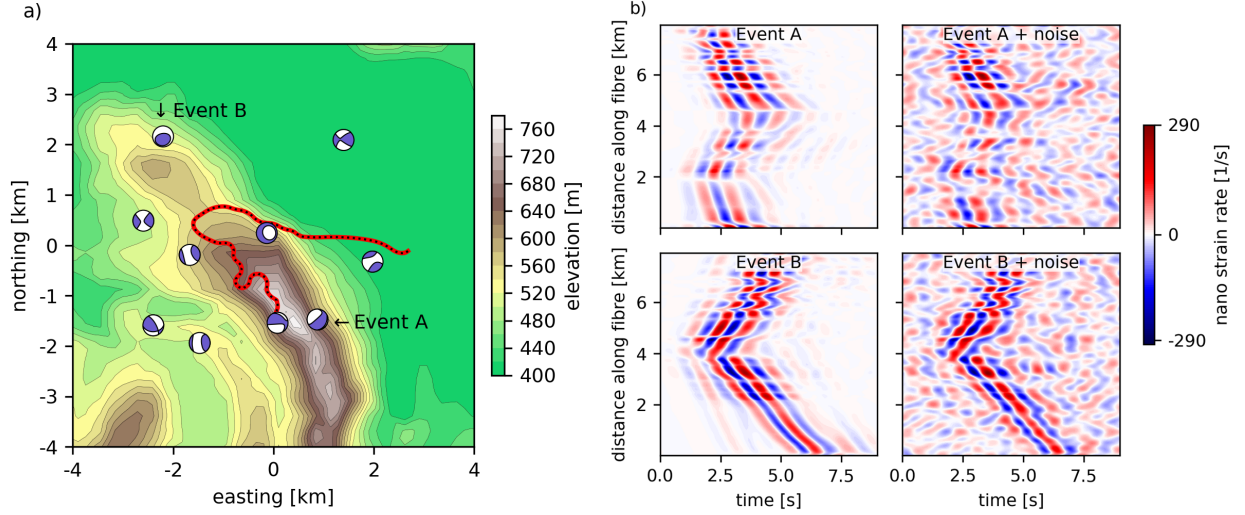


Figure 3: Setup for the synthetic tests. a) The geometry of the 8 km cable placed on top of topography. The fibre-optic cable traces a natural route up the mountain, similar to a path that a hypothetical train line or road would follow. The ten event locations and source mechanisms used for the tomography are indicated with their beach ball. Event depths are at a maximum depth of 500 m below sea level. Source inversions are presented for events A and B. b) Artificial observations for event A and event B with and without noise. In the data including noise, the signal has a maximum SNR of 10, and the noise field is coherent over 500 m along the fibre.

The update directions from gradients are computed with a trust-region based L-BFGS (Nocedal, 1980) algorithm, which is widely used in seismic FWI problems (e.g. Modrak & Tromp, 2016; Cui et al., 2024; Rodgers et al., 2024; Thrastarson et al., 2024).

In the following paragraphs, we apply the FWI routine to source inversions and tomography, describing results from DAS and IFOS datasets.

3.2 Source inversion

Throughout the source inversion, we treat V_P and V_S structures as known. To obtain a starting source model, we randomly offset the source location and time that produced the artificial data with a standard deviation of 300 m and 0.15 s, respectively. This step imitates prior information about the source. We assume to have no prior information about the moment tensor except a magnitude estimate for which we randomise the starting radiation pattern.

In our synthetic tests, we apply a misfit kernel based on the time- and frequency-dependent phase difference (Fichtner et al., 2009). We found it more effective than the L_2 -misfit in quantifying the phase differences caused by a shift in the source location. Moreover, amplitude information of real DAS systems are often affected by local effects such as the coupling of the fibre with the ground and, therefore, absolute amplitudes are challenging to model (e.g. Hudson et al., 2025). To preferably match high amplitude channels, we introduce an amplitude-dependent channel weighting in our objective function as a form of regularisation. Additionally, we window each trace such that only 2 s before and 4 s after its maximum amplitude contribute to the misfit. We inject prior knowledge into the inversion by introducing a covariance matrix that effectively introduces inter-parameter scaling, where higher uncertainties lead to larger model updates for the corresponding parameters. The covariance matrix is consistent with the randomisation of the ground truth model that produced the starting model.

Distributed acoustic sensing

The results for the noise-free event A are summarised in Fig. 4. Event A is located relatively close to the cable in the southeastern quadrant. Through the inversion, the waveforms are almost perfectly replicated by the model (Fig. 4b). Correspondingly, the source mechanism, location, and source time closely match the ground truth values. Most of the 220 m offset between the starting model and ground truth locations are recovered within the first few iterations (Fig. 4c), while corrections in depth take longer (Fig. 4d). The source time is adjusted towards the correct value within a few iterations and the moment tensor is recovered after the first iteration.

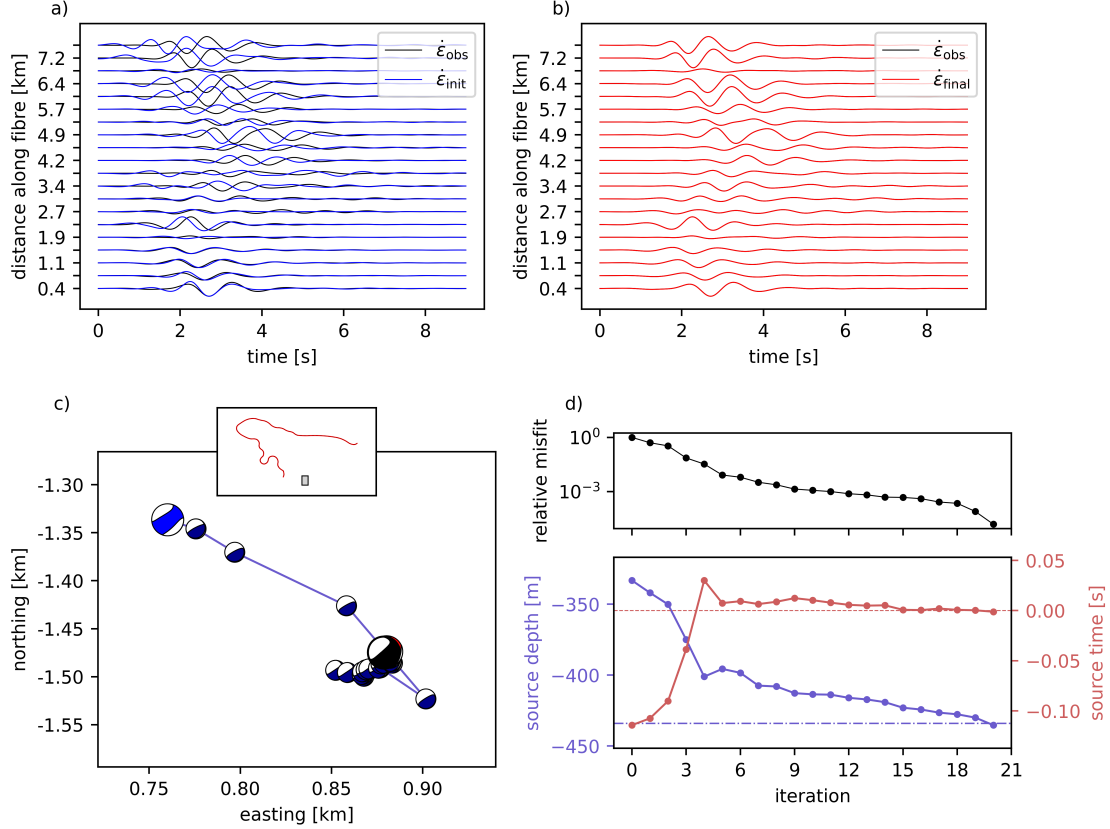


Figure 4: Source inversion with DAS for event A without noise. a) Trace-by-trace comparison of the starting waveforms to the artificial observations for 20 equally spaced DAS channels. b) The comparison of the final model against the artificial observations. c) The model for moment tensor and horizontal location throughout the inversion, starting from the blue moment tensor. The red moment tensor is the final model, which is almost entirely covered by the black beach ball that indicates the true location and radiation pattern. Smaller moment tensors are connected with lines and identify models throughout the inversion. The grey box in the overview map with the DAS cable (red) displays the limits of the zoomed-in region relative to the cable. d) The time-frequency phase misfit and the source parameters depth (blue) and time (red) per iteration, where dashed horizontal lines indicate the ground truth values.

Next, we repeat the inversion with the same starting model for the data set with noise. The associated information loss prevents a similarly good recovery of source information when compared to the ground truth (see Fig. 5). As in the noise-free case, the epicentre can be approximated to within 25 m within few iterations, and the source time can be accurately adjusted. The moment tensor, while being visually distinct from the ground truth, refers to a similar source mechanism.

Integrated strain sensing

We repeat the source inversion for event A using IFOS data with the same starting model. The inversion results are summarised in Figs. 6a-c. The inversion successfully matches the observed waveform, despite the initial waveforms being offset by nearly half a period. Overall, the behaviour of model updates is very similar to the DAS example in Fig. 4, with the horizontal location and moment tensors moving within close range to the ground truth within the first few iterations. The source depth and time parameters require more iterations but are recovered successfully as well. In contrast to the DAS inversion, there is a difference between the final model and the ground truth, with a slightly rotated moment tensor and a location that is off by a few tens of metres.

To present a more challenging example of IFOS data, we investigate event B, which is located outside the fibre-aperture (see Fig. 3). The inversion yields a model that significantly differs from the ground truth (see Figs. 6d-f), although it largely replicates the phase information of the artificial data. The final location is off by about 70 m and the radiation pattern of the source is visibly distinct in the beach ball representation. The apparent trade-off between location and

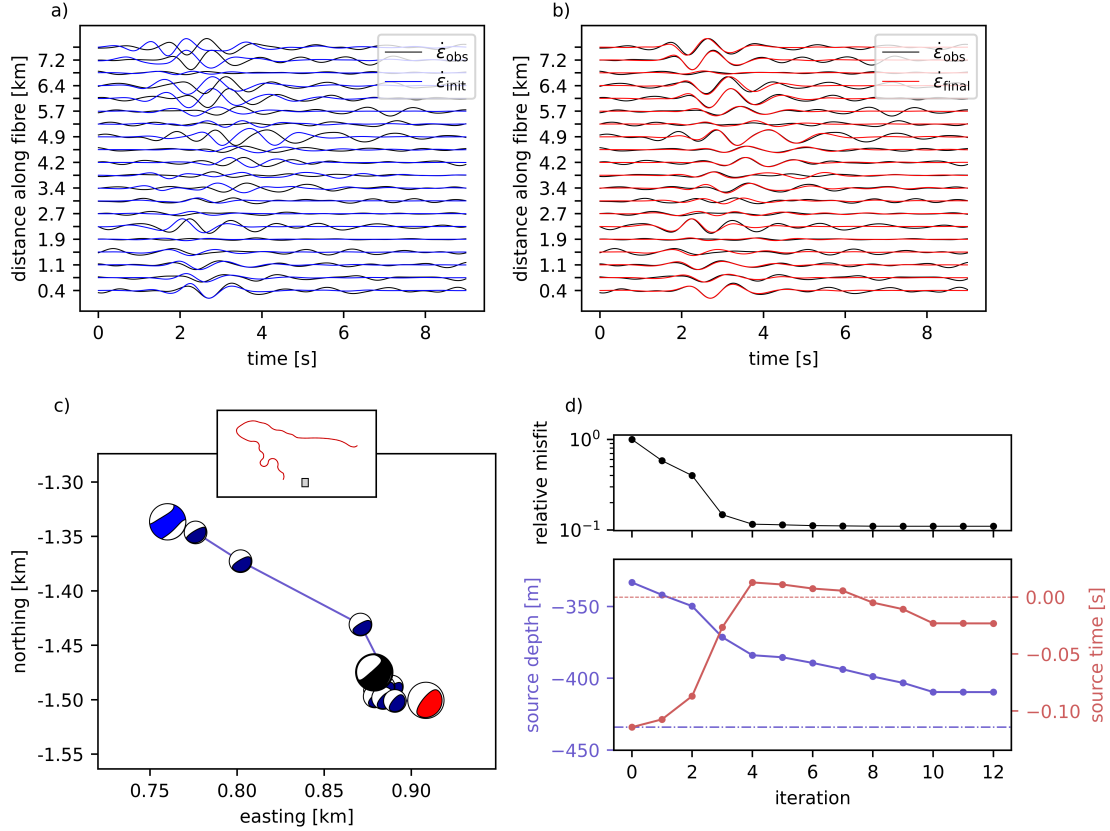


Figure 5: Source inversion with DAS for event A with noise. a) Trace-by-trace comparison of the starting model against the perturbed artificial data. b) Comparison of best-fitting model and the artificial observations. c) Horizontal location and moment tensor models throughout the inversions, from the start (blue) to the final model (red). The ground truth is indicated in black. d) The misfit improvement, source depth and time per iteration, where the horizontal dashed line indicates the ground truth.

origin time cannot be resolved with this single trace. The source inversions for event B using DAS data with and without noise present successful recoveries of the moment tensor while the location of the event is challenging to obtain (appendix C).

3.3 Tomography

In the following, we investigate to what extent the subsurface wave speeds can be resolved with DAS and IFOS given the cable geometry and events shown in Fig. 3(a). The ground truth includes checkerboard-pattern anomalies in both V_P and V_S with different length scales. The artificial data for 10 earthquakes are produced using the 1-D background model presented in Fig. 8 with 3-D checkerboard anomalies in place (Fig. 7, first column). The starting model in all inversions is the background model without anomalies. The 10 source models are assumed to be known to analyse the tomographic image without the imprint from erroneous earthquake sources.

As before in the source inversion, we base the objective function on differences in the time- and frequency-dependent phases and introduce an amplitude-dependent channel weighting. We remove source and receiver imprints by setting the kernels to zero within a radius of 100 m around their respective locations. Moreover, we smooth the sum of event kernels with averaging lengths of a quarter of the wavelength to create the final gradient. Fig. 7 summarises all final wave speed models, and the waveforms are presented in Fig. 11.

Distributed acoustic sensing

The second column in Fig. 7 presents the results of the tomography with noise-free DAS data. Over 44 iterations, the misfit improved by a factor of 50. The resulting computed waveforms match the artificial observations almost

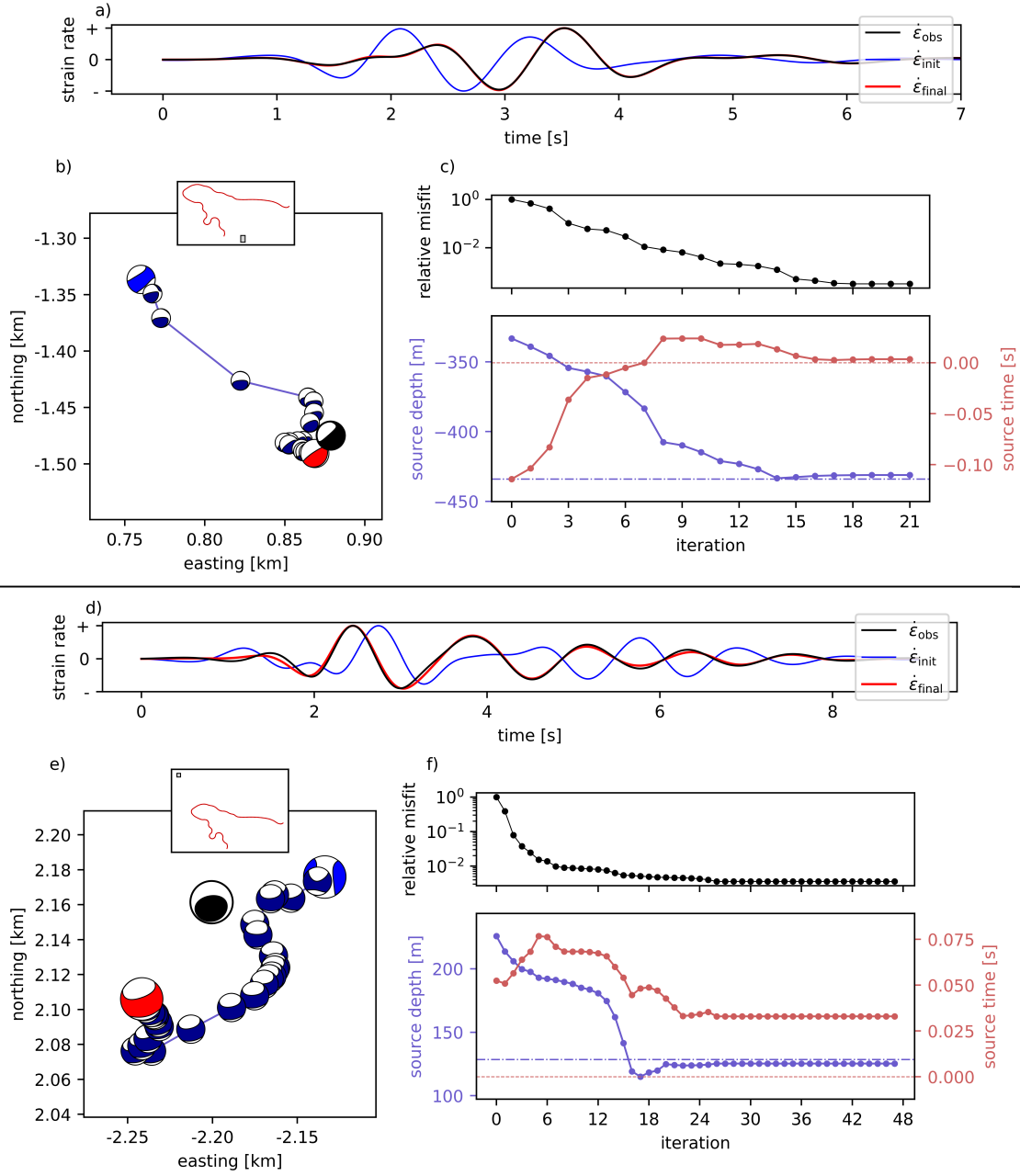


Figure 6: Source inversion with IFOS data. Panels a–c present event A with the same starting model. The final location is accurate within 25 m, and the radiation pattern largely agrees with the ground truth. The correct model parameters cannot be precisely recovered for event B (panels d–f). Despite an apparent phase match of waveforms, the inversion is unable to further improve the model parameters towards the true solution.

perfectly (see Fig. 11b). Near the cable, all V_S - anomalies are successfully recovered. At the surface ($Z = 300$ m), smearing only occurs outside the direct paths between sources and the fibre. The polarity switches of the checkerboard anomalies with depth are recovered in the vertical profiles beneath the cable. Further, we show the recovery of a similar checkerboard pattern in the image for V_P (Fig. 7, fourth row). The near surface anomalies are correctly identified as either fast or slow and deeper structures are identified with the correct polarity switches.

We repeat the experiment with the same starting model and earthquakes for DAS data with noise. Over 26 iterations, the misfit is reduced by 24%. This comparably small reduction with respect to the noise-free example is indicative of how the coherent noise field obscures the information in the artificial data (see Fig. 11d). The model is presented in the third column of Fig. 7. The noisy measurements notably deteriorate the image compared to the noise-free example. Near the surface ($Z = 300$ m) and the fibre, many of the anomalies are correctly identified nonetheless, with a notable outlier at the eastern end of the cable at $(E, N) = (2500 \text{ m}, 500 \text{ m})$. There are many erroneous structures in the final image, but the rate of correctly mapped checkerboard polarities is high, even at greater depths. In our example with noise, V_P -anomalies are only partly recovered.

Integrated strain sensing

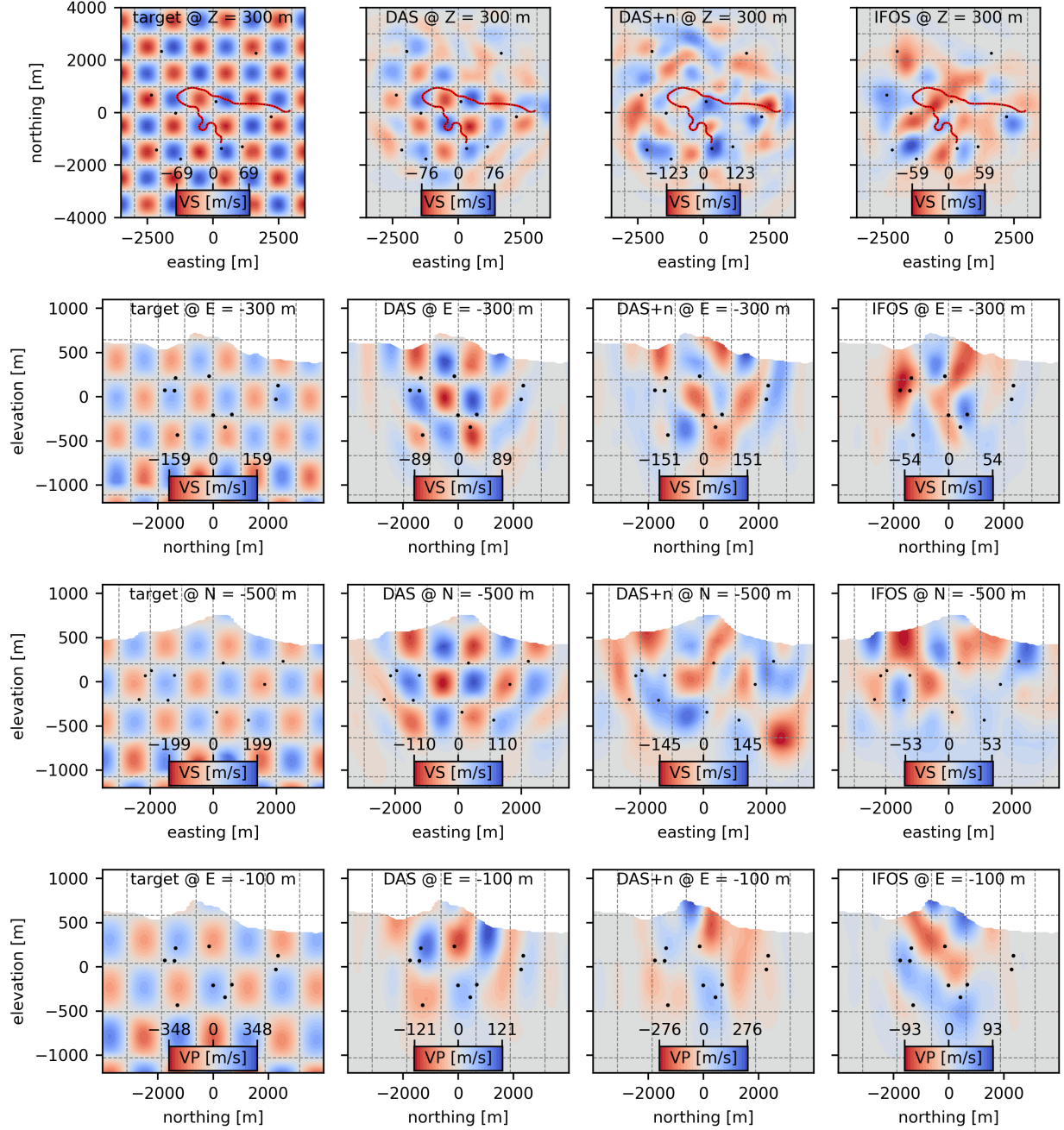
We repeat the same experiment for IFOS data. Therefore, this inversion of the subsurface is based on a total of 10 seismic traces, one for each of the 10 seismic events. The entire dataset is presented in Fig. 11(e). The inversion was performed over a total of 50 iterations with an improvement of the misfit by a factor of 500. At this stage, all computed measurements nearly perfectly match the artificial observations, as can be seen in Fig. 11(f). Comparing the target and reconstructed models (Fig. 7, 1st and 4th columns), the rate of correctly mapped anomalies is higher in the western half of the domain compared to the eastern half. In the western half, V_S -anomalies at the surface as well as in deeper area are resolved. Nevertheless, many anomalies are either misplaced or appear with the wrong polarity in the IFOS tomographic image in the eastern half of the domain.

4 Discussion

In this study, we show the potential of DAS and IFOS for source and structural inversions with FWI by comparing inversion results with the ground truth in synthetic test cases. We demonstrate that the FWI framework can overcome several challenges associated with fibre-optic data, including varying orientation, measurement of strain instead of displacement, and distributed sensitivity over the gauge length. This is besides well-known challenges addressed by numerical wave propagation modelling, such as complex media, topography, coupled viscoacoustic and viscoelastic rheologies, and the ability to bypass the need for precise picking of seismic phase arrivals, as the full waveform can be evaluated.

We present an example where FWI with DAS data recovers all parameters of a moment tensor point source even when perturbing the measurements with strong coherent noise. For an event outside the cable geometry, we successfully invert for the moment tensor, but resolving the exact location of the epicentre is difficult (see Appendix C). These positive results suggest applications of source inversions with DAS data e.g. for earthquake characterisation, monitoring icequakes on glaciers, volcanic tremors, or for induced seismicity on faults. In all cases, a better understanding of seismic sources is crucial for monitoring the dynamics of these systems, and full-waveform modelling can account for the often complex cable geometries, topography, and structural changes that aid in constraining the seismic source (Simutè et al., 2023; Doody et al., 2025). In our tomographic example, the noise-free DAS test demonstrates the theoretical imaging capability of the given fibre with known active seismic sources. The results show accurate anomaly mappings across the domain. Crucially, there is no significant loss of quality with depth. This illustrates that DAS, which measures near-horizontal strain at the surface, may enable imaging well below the surface. Even with strong added noise to the artificial observations, many of the anomalies can be correctly identified. This test opens real-data tomographic applications for FWI imaging with DAS data. For instance, the seismic hazard community benefits from high-resolution tomographic images in dense urban areas that could be obtained using existing fibre-optic networks. Moreover, DAS in volcanic environments could be used to detect and monitor the evolution of subsurface magma intrusions.

For IFOS data, various seismic phases arrive on different cable segments simultaneously, with their contribution to the integrated signal depending on the polarity relative to the local cable curvature (Fichtner et al., 2022b), which makes the data complex to interpret. We show how to account for these effects with full-waveform simulations. The successful source inversions indicate that IFOS data can contribute to constraining source characteristics of events (Müller et al., 2024), although it might fail to constrain parameters in more challenging inversions where DAS data would succeed, as demonstrated by source inversions for event B (see Appendix C). Nevertheless, a network of seismometers for tsunami early warning could be supported by subsea cables, which may be cost-effective for interrogation using



IFOS. While the tomographic image produced with noise-free IFOS measurements does not exactly replicate the ground truth, our results indicate that information about the subsurface can be extracted from IFOS measurements. The increased number of curvature points in the western half of our fibre geometry translates directly into higher resolution of the subsurface. On the global scale, both IFOS and DAS could provide new seismic data types around the world (Wuestefeld et al., 2023) and from difficult-to-access areas, such as the ocean floors (Marra et al., 2018; Donadello et al., 2024), potentially facilitating the development of a new generation of global tomographic models when combined with existing seismometer recordings.

Although we aimed to address as many complexities as possible, not all factors are modelled within our numerical simulations. We do not explicitly model the coupling of the cable to the medium, as in the forward modelling of Celli et al. (2024). None of our synthetic inversions rely on absolute amplitudes in their misfit kernel, partially mitigating this issue. However, it has been shown that poor coupling not only influences the absolute amplitudes of DAS measurements but may also alter the shape of the measured waveforms (Celli et al., 2024), a problem not addressed in our current method. Moreover, the strain field has been shown to be sensitive to small-scale heterogeneities in the subsurface (Capdeville & Sladen, 2024). Depending on the dataset, these challenges may require modifications to our method.

5 Conclusions

The motivation for this study is the emerging availability of high-quality data from fibre-optic sensing over the past decade. We have provided the theoretical framework to perform FWI with DAS and IFOS, and demonstrate its potential through synthetic tests incorporating several complex factors. The adjoint sources for fibre-optic measurements are oriented moment tensor sources, where the source-time function is shared among all discretisation points along the gauge length of a channel. We apply these findings to invert for the source and subsurface structure in synthetic test cases with the final models compared to the ground truth. We find that the artificial DAS measurements constrain the source model reliably for an event near the cable, and even the IFOS inversion recovers the source parameters for this event.

Our noise-free tomography with known earthquake sources indicates the potential imaging capability of DAS data, where we see that the measurements are sensitive to large parts of the subsurface structure, including depth resolution. The tomographic image is notably distorted by strong noise added to the DAS data, but many anomalies can still be correctly identified. We show that tomography with IFOS data is theoretically possible, especially with high-curvatures of the fibre.

This study lays the foundation for real-data applications of FWI with fibre-optic data. We see potential uses of these methods in environmental monitoring, seismic hazard analysis in urban areas, tsunami early-warning systems, and global tomography.

Acknowledgments

S.N. gratefully acknowledges funding provided by the European Union’s Horizon 2020 research and innovation program under the Marie Skłodowska-Curie grant agreement No. 955515 (SPIN ITN). We would like to express our sincere thanks to Christian Böhm and Scott Keating for their valuable discussions and input during the development of this study.

Data Availability

The software package *Pyber* is openly accessible at www.gitlab.com/swp_ethz/public/pyber. It communicates with the spectral-element wave propagation solver *Salvus* (Afanasyev et al., 2019) to place the fibre within the simulation mesh, evaluate the strain along the cable, and automate the inversion workflow for source and subsurface parameters. The codes are readily available with tutorials for how to run forward simulations and how to perform source inversions and tomographies. The workflow is flexible and supports arbitrary fibre geometries and scales.

References

Abukrat, Y., Sinitsyn, P., Reshef, M., & Lellouch, A., 2023. Applications and limitations of distributed acoustic sensing in shallow seismic surveys and monitoring, *Geophysics*, **88**(6), WC1–WC12.

- Afanasiev, M., Boehm, C., van Driel, M., Krischer, L., Rietmann, M., May, D. A., Knepley, M. G., & Fichtner, A., 2019. Modular and flexible spectral-element waveform modelling in two and three dimensions, *Geophysical Journal International*, **216**(3), 1675–1692.
- Azzola, J., Thiemann, K., & Gaucher, E., 2023. Integration of distributed acoustic sensing for real-time seismic monitoring of a geothermal field, *Geothermal Energy*, **11**, 30.
- Berti, S., Aleardi, M., & Stucchi, E., 2024. A probabilistic full waveform inversion of surface waves, *Geophysical Prospecting*, **72**, 3448–3473.
- Biondi, E., Zhu, W., Li, J., Williams, E. F., & Zhan, Z., 2023. An upper-crust lid over the Long Valley magma chamber, *Science Advances*, **9**(42), eadi9878.
- Bogris, A., Nikas, T., Simos, C., Simos, I., Lentas, K., Melis, N. S., Fichtner, A., Bowden, D., Smolinski, K., Mesaritakis, C., et al., 2022. Sensitive seismic sensors based on microwave frequency fiber interferometry in commercially deployed cables, *Scientific Reports*, **12**, 14000.
- Borisov, D., Gao, F., Williamson, P., & Tromp, J., 2020. Application of 2D full-waveform inversion on exploration land data, *Geophysics*, **85**(2), R75–R86.
- Bowden, D. C., Fichtner, A., Nikas, T., Bogris, A., Simos, C., Smolinski, K., Koroni, M., Lentas, K., Simos, I., & Melis, N. S., 2022. Linking distributed and integrated fiber-optic sensing, *Geophysical Research Letters*, **49**(16), e2022GL098727.
- Capdeville, Y. & Sladen, A., 2024. DAS sensitivity to heterogeneity scales much smaller than the minimum wavelength, *Seismica*, **3**(1).
- Celli, N. L., Bean, C. J., & O’Brien, G. S., 2024. Full-waveform simulation of DAS records, response and cable-ground coupling, *Geophysical Journal International*, **236**(1), 659–674.
- Cui, C., Lei, W., Liu, Q., Peter, D., Bozdağ, E., Tromp, J., Hill, J., Podhorszki, N., & Pugmire, D., 2024. GLAD-M35: a joint P and S global tomographic model with uncertainty quantification, *Geophysical Journal International*, **239**(1), 478–502.
- Currenti, G., Jousset, P., Napoli, R., Krawczyk, C., & Weber, M., 2021. On the comparison of strain measurements from fibre optics with dense seismometer array at Etna volcano (Italy), *Solid Earth Discussions*, **2021**, 1–19.
- Donadello, S., Clivati, C., Govoni, A., Margheriti, L., Vassallo, M., Brenda, D., Hovsepyan, M., Bertacco, E. K., Concas, R., Levi, F., et al., 2024. Seismic monitoring using the telecom fiber network, *Communications Earth & Environment*, **5**(1), 178.
- Doody, C., Rodgers, A., Chiang, A., Afanasiev, M., Boehm, C., Krischer, L., & Simmons, N., 2025. Improved earthquake source parameters with 3D wavespeed models in California and Nevada, *Seismological Research Letters*, **96**(1), 499–509.
- Eaid, M. V., Keating, S. D., Innanen, K. A., Macquet, M., & Lawton, D., 2023. Field assessment of elastic full-waveform inversion of combined accelerometer and distributed acoustic sensing data in a vertical seismic profile configuration, *Geophysics*, **88**(6), WC163–WC180.
- Ehsaninezhad, L., Wollin, C., Rodríguez Tribaldos, V., Schwarz, B., & Krawczyk, C. M., 2024. Urban subsurface exploration improved by denoising of virtual shot gathers from distributed acoustic sensing ambient noise, *Geophysical Journal International*, **237**(3), 1751–1764.
- Faccioli, E., Maggio, F., Paolucci, R., & Quarteroni, A., 1997. 2D and 3D elastic wave propagation by a pseudo-spectral domain decomposition method, *Journal of seismology*, **1**, 237–251.
- Fang, G., Li, Y. E., Zhao, Y., & Martin, E. R., 2020. Urban near-surface seismic monitoring using distributed acoustic sensing, *Geophysical Research Letters*, **47**(6), e2019GL086115.
- Fichtner, A. & Igel, H., 2009. Sensitivity densities for rotational ground-motion measurements, *Bulletin of the Seismological Society of America*, **99**(2B), 1302–1314.
- Fichtner, A., Bunge, H.-P., & Igel, H., 2006. The adjoint method in seismology: I. Theory, *Physics of the Earth and Planetary Interiors*, **157**(1-2), 86–104.
- Fichtner, A., Kennett, B. L., Igel, H., & Bunge, H.-P., 2009. Full seismic waveform tomography for upper-mantle structure in the Australasian region using adjoint methods, *Geophysical Journal International*, **179**(3), 1703–1725.
- Fichtner, A., Bogris, A., Bowden, D., Lentas, K., Melis, N. S., Nikas, T., Simos, C., Simos, I., & Smolinski, K., 2022a. Sensitivity kernels for transmission fibre optics, *Geophysical Journal International*, **231**(2), 1040–1044.

- Fichtner, A., Bogris, A., Nikas, T., Bowden, D., Lentas, K., Melis, N. S., Simos, C., Simos, I., & Smolinski, K., 2022b. Theory of phase transmission fibre-optic deformation sensing, *Geophysical Journal International*, **231**(2), 1031–1039.
- Fichtner, A., Hofstede, C., Gebraad, L., Zunino, A., Zigone, D., & Eisen, O., 2023. Borehole fibre-optic seismology inside the Northeast Greenland Ice Stream, *Geophysical Journal International*, **235**(3), 2430–2441.
- Hudson, T., Stork, A., Muir, J., & Fichtner, A., 2025. Unlocking DAS amplitude information through coherency coupling quantification, *Seismica*, **4**(1).
- Hudson, T. S., Baird, A. F., Kendall, J.-M., Kufner, S.-K., Brisbourne, A. M., Smith, A. M., Butcher, A., Chalari, A., & Clarke, A., 2021. Distributed acoustic sensing (DAS) for natural microseismicity studies: A case study from Antarctica, *Journal of Geophysical Research: Solid Earth*, **126**(7), e2020JB021493.
- Igel, J. K. H., Klaasen, S., Noe, S., Nomikou, P., Karantzaos, K., & Fichtner, A., 2024. Challenges in Submarine Fiber-Optic Earthquake Monitoring, *Journal of Geophysical Research: Solid Earth*, **129**(12), e2024JB029556.
- Jousset, P., Currenti, G., Schwarz, B., Chalari, A., Tilmann, F., Reinsch, T., Zuccarello, L., Privitera, E., & Krawczyk, C. M., 2022. Fibre optic distributed acoustic sensing of volcanic events, *Nature communications*, **13**(1), 1753.
- Kang, J., Walter, F., Paitz, P., Aichele, J., Edme, P., Meier, L., & Fichtner, A., 2024. Automatic monitoring of rock-slope failures using distributed acoustic sensing and semi-supervised learning, *Geophysical Research Letters*, **51**(19), e2024GL110672.
- Katakami, S., Korenaga, M., Iwata, N., Araki, E., Takahashi, N., & Noda, S., 2025. Immediate and high-precision hypocentral determination for earthquake early warning applications using distributed acoustic sensing, *Bulletin of the Seismological Society of America*, **115**(1), 174–190.
- Kennett, B. L., 2024. *A Guide to the Seismic Wavefield as seen by DAS*, The Australian National University, Chapter 3.5.
- Kim, Y., Liu, Q., & Tromp, J., 2011. Adjoint centroid-moment tensor inversions, *Geophysical Journal International*, **186**(1), 264–278.
- Klaasen, S., Paitz, P., Lindner, N., Dettmer, J., & Fichtner, A., 2021. Distributed acoustic sensing in volcano-glacial environments—Mount Meager, British Columbia, *Journal of Geophysical Research: Solid Earth*, **126**(11), e2021JB022358.
- Klaasen, S., Thrastarson, S., Çubuk-Sabuncu, Y., Jónsdóttir, K., Gebraad, L., Paitz, P., & Fichtner, A., 2023. Subglacial volcano monitoring with fibre-optic sensing: Grímsvötn, Iceland, *Volcanica*, **6**(2), 301–311.
- Komatitsch, D. & Vilotte, J.-P., 1998. The spectral element method: an efficient tool to simulate the seismic response of 2D and 3D geological structures, *Bulletin of the seismological society of America*, **88**(2), 368–392.
- Lailly, P., 1983. The seismic inverse problem as a sequence of before stack migrations, *Conference on Inverse Scattering—Theory and Application*, pp. edited by J. Bednar, R. Redner, E. Robinson, and A. Weglein, Soc. Industr. appl. Math., Philadelphia, PA.
- Lei, W., Ruan, Y., Bozdağ, E., Peter, D., Lefebvre, M., Komatitsch, D., Tromp, J., Hill, J., Podhorszki, N., & Pugmire, D., 2020. Global adjoint tomography—model GLAD-M25, *Geophysical Journal International*, **223**(1), 1–21.
- Lekić, V. & Romanowicz, B., 2011. Inferring upper-mantle structure by full waveform tomography with the spectral element method, *Geophysical Journal International*, **185**(2), 799–831.
- Lellouch, A., Yuan, S., Spica, Z., Biondi, B., & Ellsworth, W. L., 2019. Seismic velocity estimation using passive downhole distributed acoustic sensing records: Examples from the San Andreas fault observatory at depth, *Journal of Geophysical Research: Solid Earth*, **124**(7), 6931–6948.
- Lentas, K., Bowden, D., Melis, N., Fichtner, A., Koroni, M., Smolinski, K., Bogris, A., Nikas, T., Simos, C., & Simos, I., 2023. Earthquake location based on distributed acoustic sensing (DAS) as a seismic array, *Physics of the Earth and Planetary Interiors*, **344**, 107109.
- Li, J., Kim, T., Lapusta, N., Biondi, E., & Zhan, Z., 2023. The break of earthquake asperities imaged by distributed acoustic sensing, *Nature*, **620**(7975), 800–806.
- Li, Z. & Zhan, Z., 2018. Pushing the limit of earthquake detection with distributed acoustic sensing and template matching: A case study at the Brady geothermal field, *Geophysical Journal International*, **215**(3), 1583–1593.
- Lior, I., Mercierat, E. D., Rivet, D., Sladen, A., & Ampuero, J.-P., 2022. Imaging an underwater basin and its resonance modes using optical fiber distributed acoustic sensing, *Seismological Society of America*, **93**(3), 1573–1584.

- Liu, C., Banerjee, R., Grand, S. P., Sandvol, E., Mitra, S., Liang, X., & Wei, S., 2024. A high-resolution seismic velocity model for East Asia using full-waveform tomography: Constraints on India-Asia collisional tectonics, *Earth and Planetary Science Letters*, **639**, 118764.
- Liu, Q. & Tromp, J., 2006. Finite-frequency kernels based on adjoint methods, *Bulletin of the Seismological Society of America*, **96**(6), 2383–2397.
- Liu, Q., Polet, J., Komatitsch, D., & Tromp, J., 2004. Spectral-element moment tensor inversions for earthquakes in southern california, *Bulletin of the Seismological Society of America*, **94**(5), 1748–1761.
- Luo, B., Jin, G., & Stanek, F., 2021a. Near-field strain in distributed acoustic sensing-based microseismic observation, *Geophysics*, **86**(5), P49–P60.
- Luo, B., Lellouch, A., Jin, G., Biondi, B., & Simmons, J., 2021b. Seismic inversion of shale reservoir properties using microseismic-induced guided waves recorded by distributed acoustic sensing, *Geophysics*, **86**(4), R383–R397.
- Marra, G., Clivati, C., Luckett, R., Tampellini, A., Kronjäger, J., Wright, L., Mura, A., Levi, F., Robinson, S., Xuereb, A., et al., 2018. Ultrastable laser interferometry for earthquake detection with terrestrial and submarine cables, *Science*, **361**(6401), 486–490.
- Marra, G., Fairweather, D., Kamalov, V., Gaynor, P., Cantono, M., Mulholland, S., Baptie, B., Castellanos, J., Vagenas, G., Gaudron, J.-O., et al., 2022. Optical interferometry-based array of seafloor environmental sensors using a transoceanic submarine cable, *Science*, **376**(6595), 874–879.
- Martin, E. R., Lindsey, N. J., Ajo-Franklin, J. B., & Biondi, B. L., 2021. Introduction to interferometry of fiber-optic strain measurements, *Distributed acoustic sensing in geophysics: Methods and applications*, pp. 111–129.
- Modrak, R. & Tromp, J., 2016. Seismic waveform inversion best practices: regional, global and exploration test cases, *Geophysical Journal International*, **206**(3), 1864–1889.
- Modrak, R. T., Borisov, D., Lefebvre, M., & Tromp, J., 2018. SeisFlows—Flexible waveform inversion software, *Computers & geosciences*, **115**, 88–95.
- Müller, N., Noe, S., Husmann, D., Morel, J., & Fichtner, A., 2024. Earthquake source inversion by integrated fiber-optic sensing, *Seismica*, **3**(2).
- Nishimura, T., Emoto, K., Nakahara, H., Miura, S., Yamamoto, M., Sugimura, S., Ishikawa, A., & Kimura, T., 2021. Source location of volcanic earthquakes and subsurface characterization using fiber-optic cable and distributed acoustic sensing system, *Scientific reports*, **11**(1), 6319.
- Nocedal, J., 1980. Updating quasi-Newton matrices with limited storage, *Mathematics of computation*, **35**(151), 773–782.
- Noe, S., Husmann, D., Müller, N., Morel, J., & Fichtner, A., 2023. Long-range fiber-optic earthquake sensing by active phase noise cancellation, *Scientific reports*, **13**(1), 13983.
- Ouellet, S. M., Dettmer, J., Lato, M. J., Cole, S., Hutchinson, D. J., Karrenbach, M., Dashwood, B., Chambers, J. E., & Crickmore, R., 2024. Previously hidden landslide processes revealed using distributed acoustic sensing with nanostrain-rate sensitivity, *Nature Communications*, **15**(1), 6239.
- Paitz, P., Lindner, N., Edme, P., Huguenin, P., Hohl, M., Sovilla, B., Walter, F., & Fichtner, A., 2023. Phenomenology of avalanche recordings from distributed acoustic sensing, *Journal of Geophysical Research: Earth Surface*, **128**(5), e2022JF007011.
- Piana Agostinetti, N., Villa, A., & Saccorotti, G., 2022. Distributed acoustic sensing as a tool for subsurface mapping and seismic event monitoring: A proof of concept, *Solid Earth*, **13**(2), 449–468.
- Qu, L., Pan, W., Innanen, K., Macquet, M., & Lawton, D., 2024. Feasibility study of anisotropic full-waveform inversion with DAS data in a vertical seismic profile configuration at the Newell County Facility, Alberta, Canada, *Surveys in Geophysics*, pp. 1–26.
- Rodgers, A., Doody, C., & Fichtner, A., 2024. WUS324: Multiscale full waveform inversion approaching convergence improves waveform fits while imaging seismic structure of the western United States, *Geophysical Research Letters*, **51**(20), e2024GL110911.
- Schouten, T. L. A., Gebraad, L., Noe, S., Gülcher, A. J. P., Thrastarson, S., van Herwaarden, D.-P., & Fichtner, A., 2024. Full-waveform inversion reveals diverse origins of lower mantle positive wave speed anomalies, *Scientific Reports*, **14**(1), 26708.
- Simutè, S., Boehm, C., Krischer, L., Gokhberg, A., Vallée, M., & Fichtner, A., 2023. Bayesian seismic source inversion with a 3-D Earth model of the Japanese Islands, *Journal of Geophysical Research: Solid Earth*, **128**(1), e2022JB024231.

- Smolinski, K. T., Bowden, D. C., Paitz, P., Kugler, F., & Fichtner, A., 2024. Shallow subsurface imaging using challenging urban DAS data, *Seismological Research Letters*, **96**(1), 168–181.
- Spica, Z. J., Castellanos, J. C., Viens, L., Nishida, K., Akuhara, T., Shinohara, M., & Yamada, T., 2022. Subsurface imaging with ocean-bottom distributed acoustic sensing and water phases reverberations, *Geophysical Research Letters*, **49**(2), e2021GL095287.
- Tarantola, A., 1984. Inversion of seismic reflection data in the acoustic approximation: Geophysics, *Geophysics*, **49**(8), 1259–1266.
- Thrustarson, S., van Herwaarden, D.-P., Noe, S., Josef Schiller, C., & Fichtner, A., 2024. REVEAL: A global full-waveform inversion model, *Bulletin of the Seismological Society of America*, **114**(3), 1392–1406.
- Tromp, J., 2020. Seismic wavefield imaging of Earth’s interior across scales, *Nature Reviews Earth & Environment*, **1**(1), 40–53.
- Tromp, J., Tape, C., & Liu, Q., 2005. Seismic tomography, adjoint methods, time reversal and banana-doughnut kernels, *Geophysical Journal International*, **160**(1), 195–216.
- Tuinstra, K., Grigoli, F., Lanza, F., Rinaldi, A. P., Fichtner, A., & Wiemer, S., 2024. Locating clustered seismicity using Distance Geometry Solvers: applications for sparse and single-borehole DAS networks, *Geophysical Journal International*, **238**(2), 661–680.
- Vera Rodriguez, I. & Wuestefeld, A., 2020. Strain microseisms: Radiation patterns, synthetics, and moment tensor resolvability with distributed acoustic sensing in isotropic media, *Geophysics*, **85**(3), KS101–KS114.
- Virieux, J. & Operto, S., 2009. An overview of full-waveform inversion in exploration geophysics, *Geophysics*, **74**(6), WCC1–WCC26.
- Walter, F., Gräff, D., Lindner, F., Paitz, P., Köpfl, M., Chmiel, M., & Fichtner, A., 2020. Distributed acoustic sensing of microseismic sources and wave propagation in glaciated terrain, *Nature communications*, **11**(1), 2436.
- Wuestefeld, A., Spica, Z. J., Aderhold, K., Huang, H.-H., Ma, K.-F., Lai, V. H., Miller, M., Urmantseva, L., Zapf, D., Bowden, D. C., et al., 2023. The global DAS month of February 2023, *Seismological Research Letters*, **95**, 1569–1577.
- Yin, J., Soto, M. A., Ramírez, J., Kamalov, V., Zhu, W., Husker, A., & Zhan, Z., 2023. Real-data testing of distributed acoustic sensing for offshore earthquake early warning, *The Seismic Record*, **3**(4), 269–277.
- Yu, C., Zhan, Z., Lindsey, N. J., Ajo-Franklin, J. B., & Robertson, M., 2019. The potential of DAS in teleseismic studies: Insights from the Goldstone experiment, *Geophysical Research Letters*, **46**(3), 1320–1328.
- Yust, M. B., Cox, B. R., Vantassel, J. P., Hubbard, P. G., Boehm, C., & Krischer, L., 2023. Near-surface 2D imaging via FWI of DAS data: An examination on the impacts of FWI starting model, *Geosciences*, **13**(3), 63.
- Zhan, Z., Cantono, M., Kamalov, V., Mecozzi, A., Müller, R., Yin, S., & Castellanos, J. C., 2021. Optical polarization-based seismic and water wave sensing on transoceanic cables, *Science*, **371**(6532), 931–936.

A Derivation of adjoint equation for source and tomographic parameters

We show that the adjoint equation in eq. (10) holds for source and tomographic parameter inversions and remains unchanged when considering strain as the observable in the objective function χ .

Given the wave-field operator L and a source term f that depend on the wave speed model \mathbf{m}_v and earthquake source parameters \mathbf{m}_s , respectively, the wavefield \mathbf{u} is subject to the following equation (see eq. (8)):

$$L(\mathbf{u}; \mathbf{m}_v, \mathbf{x}, t) = f(\mathbf{m}_s; \mathbf{x}, t) \quad (23)$$

For conciseness, we introduce the scalar product defined on the spatial Ω and temporal interval between start and end time $[t_0, t_1]$ as

$$\langle f, g \rangle := \int_{t_0}^{t_1} \int_{\Omega} f \cdot g d\Omega dt. \quad (24)$$

We aim to optimise the general objective function in eq. (9) with changes to the model parameters. Taking the model derivative for the tomographic model of eq. (23), yields:

$$\frac{d\chi}{d\mathbf{m}_v} = \langle 1, \frac{\partial\chi}{\partial\mathbf{m}_v} + \frac{\partial\chi}{\partial\mathbf{u}} \frac{d\mathbf{u}}{d\mathbf{m}_v} \rangle \quad (25)$$

$$= \langle 1, \frac{\partial\chi}{\partial\mathbf{m}_v} + \frac{\partial\chi}{\partial\bar{\epsilon}} \frac{\partial\bar{\epsilon}}{\partial\mathbf{u}} \frac{d\mathbf{u}}{d\mathbf{m}_v} \rangle. \quad (26)$$

As the result of eq. (26) leads to the required evaluation of $\frac{d\mathbf{u}}{d\mathbf{m}_v}$, a matrix which is for realistic applications extremely expensive to compute, we seek to remove this dependency by adding a homogeneous term to both sides of the equation. For this purpose, we choose the model derivative of the original partial-differential eq. (23)

$$0 = L - f \quad (27)$$

$$= \frac{d}{d\mathbf{m}_v} (L - f) \quad (28)$$

$$= \frac{\partial L}{\partial\mathbf{u}} \frac{d\mathbf{u}}{d\mathbf{m}_v} + \frac{\partial L}{\partial\mathbf{m}_v} + \underbrace{\frac{\partial f}{\partial\mathbf{m}_v}}_{=0}. \quad (29)$$

When multiplied with a test field $\Psi = \Psi(\mathbf{x}, t)$, the term in eq. (29) remains homogeneous

$$0 = \langle \Psi, \frac{\partial L}{\partial\mathbf{u}} \frac{d\mathbf{u}}{d\mathbf{m}_v} + \frac{\partial L}{\partial\mathbf{m}_v} \rangle. \quad (30)$$

Adding the terms of eqs. (26) and (30) with the definition of the adjoint operator L^\dagger given as $\langle \mathbf{a}, L\mathbf{b} \rangle = \langle \mathbf{b}, L^\dagger \mathbf{a} \rangle$ for any given $\mathbf{a} = \mathbf{a}(\mathbf{x}, t)$ and $\mathbf{b} = \mathbf{b}(\mathbf{x}, t)$, we find:

$$\frac{d\chi}{d\mathbf{m}_v} = \langle 1, \frac{\partial\chi}{\partial\mathbf{m}_v} + \frac{\partial\chi}{\partial\bar{\epsilon}} \frac{\partial\bar{\epsilon}}{\partial\mathbf{u}} \frac{d\mathbf{u}}{d\mathbf{m}_v} \rangle + \langle \Psi, \frac{\partial L}{\partial\mathbf{u}} \frac{d\mathbf{u}}{d\mathbf{m}_v} + \frac{\partial L}{\partial\mathbf{m}_v} \rangle \quad (31)$$

$$= \langle 1, \frac{\partial\chi}{\partial\mathbf{m}_v} \rangle + \langle \frac{d\mathbf{u}}{d\mathbf{m}_v}, \underbrace{(\frac{\partial\chi}{\partial\bar{\epsilon}} \frac{\partial\bar{\epsilon}}{\partial\mathbf{u}})^\dagger + (\frac{\partial L}{\partial\mathbf{u}})^\dagger \Psi}_{=0} \rangle + \langle \Psi, \frac{\partial L}{\partial\mathbf{m}_v} \rangle \quad (32)$$

$$= \langle 1, \frac{\partial\chi}{\partial\mathbf{m}_v} \rangle + \langle \Psi, \frac{\partial L}{\partial\mathbf{m}_v} \rangle, \quad (33)$$

where eq. (32) constrains the test vector Ψ to be subject to a partial-differential equation, which is the so-called adjoint equation. This concludes the derivation of the adjoint equation for the model parameters, the derivation for the earthquake source parameters can be carried out in a similar manner. Starting with the model derivative of the

partial-differential equation and multiplication by a test function Ψ :

$$0 = L - f \quad (34)$$

$$= \frac{d}{d\mathbf{m}_s}(L - f) \quad (35)$$

$$= \frac{\partial L}{\partial \mathbf{u}} \frac{d\mathbf{u}}{d\mathbf{m}_s} + \underbrace{\frac{\partial L}{\partial \mathbf{m}_s}}_{=0} + \frac{\partial f}{\partial \mathbf{m}_s} \quad (36)$$

$$= \langle \Psi, \frac{\partial L}{\partial \mathbf{u}} \frac{d\mathbf{u}}{d\mathbf{m}_s} + \frac{\partial f}{\partial \mathbf{m}_s} \rangle \quad (37)$$

The model derivative of the objective function can be computed with the addition of eq. (37)

$$\frac{d\chi}{d\mathbf{m}_s} = \langle 1, \frac{\partial \chi}{\partial \mathbf{m}_s} + \frac{\partial \chi}{\partial \bar{\epsilon}} \frac{\partial \bar{\epsilon}}{\partial \mathbf{u}} \frac{d\mathbf{u}}{d\mathbf{m}_s} \rangle + \langle \Psi, \frac{\partial L}{\partial \mathbf{u}} \frac{d\mathbf{u}}{d\mathbf{m}_s} + \frac{\partial f}{\partial \mathbf{m}_s} \rangle \quad (38)$$

$$= \langle 1, \frac{\partial \chi}{\partial \mathbf{m}_s} \rangle + \langle \frac{d\mathbf{u}}{d\mathbf{m}_s}, \underbrace{(\frac{\partial \chi}{\partial \bar{\epsilon}} \frac{\partial \bar{\epsilon}}{\partial \mathbf{u}})^\dagger + (\frac{\partial L}{\partial \mathbf{u}})^\dagger \Psi}_{=0} \rangle + \langle \Psi, \frac{\partial f}{\partial \mathbf{m}_s} \rangle \quad (39)$$

$$= \langle 1, \frac{\partial \chi}{\partial \mathbf{m}_s} \rangle + \langle \Psi, \frac{\partial f}{\partial \mathbf{m}_s} \rangle, \quad (40)$$

which concludes the derivation for the adjoint equation to constrain earthquake source parameters in an inversion.

Hereby, we have shown that the model gradients of the objective function for tomographic and source parameters lead to the same adjoint problem

$$(\frac{\partial L}{\partial \mathbf{u}})^\dagger \Psi = -(\frac{\partial \chi}{\partial \bar{\epsilon}} \frac{\partial \bar{\epsilon}}{\partial \mathbf{u}})^\dagger \quad (41)$$

$$L^\dagger(\Psi) = -(\frac{\partial \chi}{\partial \bar{\epsilon}} \frac{\partial \bar{\epsilon}}{\partial \mathbf{u}})^\dagger, \quad (42)$$

where we identify the test field as the adjoint wavefield, i.e. $\Psi = \mathbf{u}^\dagger$. The exact nature of the source term is discussed in detail in the main text.

B Derivation of adjoint source term for strain rate

For brevity, the derivations in the main text focus on strain instead of strain rates. However, both observables can be used interchangeably in an optimisation scheme, requiring only a slight adjustment to the adjoint source time function $S(t)$.

The objective function is defined in the time interval $[t_0, t_1]$. The misfit kernel has its dependency now for the strain rate instead of strain compared to before, i.e. $h = h(\dot{\bar{\epsilon}})$. For one channel, we demonstrate that the derivative of the wavefield with respect to the objective function can be transformed as

$$\frac{\partial \chi_c}{\partial \mathbf{u}} = \int_{t_0}^{t_1} \frac{\partial h_c}{\partial \mathbf{u}} dt \quad (43)$$

$$= \int_{t_0}^{t_1} \frac{\partial h_c}{\partial \dot{\bar{\epsilon}}} \frac{\partial \dot{\bar{\epsilon}}}{\partial \mathbf{u}} dt \quad (44)$$

$$= \int_{t_0}^{t_1} \frac{\partial h_c}{\partial \dot{\bar{\epsilon}}} \frac{\partial}{\partial t} \frac{\partial \bar{\epsilon}}{\partial \mathbf{u}} dt \quad (45)$$

$$= \underbrace{\frac{\partial \bar{\epsilon}}{\partial \mathbf{u}} \frac{\partial h_c}{\partial \dot{\bar{\epsilon}}}}_{=0} \Big|_{t_0}^{t_1} - \int_{t_0}^{t_1} \frac{\partial}{\partial t} \frac{\partial h_c}{\partial \dot{\bar{\epsilon}}} \frac{\partial \bar{\epsilon}}{\partial \mathbf{u}} dt \quad (46)$$

$$= - \int_{t_0}^{t_1} \frac{\partial}{\partial t} \frac{\partial h_c}{\partial \dot{\bar{\epsilon}}} \frac{\partial \bar{\epsilon}}{\partial \mathbf{u}} dt \quad (47)$$

given that the misfit kernel is continuous and smoothly tapered at its boundaries, i.e. $h(t_0) = h(t_1) = 0$. Therefore, it holds that

$$\frac{\partial h_c}{\partial \mathbf{u}} = -\frac{\partial}{\partial t} \frac{\partial h_c}{\partial \dot{\epsilon}} \frac{\partial \bar{\epsilon}}{\partial \mathbf{u}} \quad (48)$$

in the Hilbert space defined by a product in the time integral, leading to eq. 48 as a valid starting point for the derivations in eq. (11). Following the same steps as in the main text, we obtain

$$\int_{\Omega} f_{c,k}^{\dagger} \cdot \delta \mathbf{u} d\Omega = \frac{1}{N_g} \sum_{g=0}^{N_g} \int_{\Omega} \hat{\mathbf{x}} k \delta(\mathbf{x} - \mathbf{x}_c, g) \frac{\partial}{\partial t} \frac{\partial h_c}{\partial \dot{\epsilon}} \mathbf{e} \mathbf{e}^T(\mathbf{x}) : \epsilon(\delta \mathbf{u}) d\Omega, \quad (49)$$

which, upon comparison with the general moment tensor equation in eq. 20, allows us to identify the source time function

$$S(t) = \frac{\partial}{\partial t} \frac{\partial h_c}{\partial \dot{\epsilon}}. \quad (50)$$

C Additional figures for synthetic inversions

In this appendix, we provide information about the wave speed model in terms of the 1-D layered background model (see Fig. 8). Also, we give insights into how a source inversion with DAS looks for event B, which is located outside the immediate fibre aperture. The event is located approximately 1.5 km away from the nearest point on the cable, in the northwestern quadrant of the domain (see Fig. 9). The starting moment tensor is significantly different from the ground truth source mechanism, and the epicentre is initially assumed to be 100 m shallower than the true location. The starting model produces waveforms that significantly differ from the data in terms of polarity. In the noise-free example, a model that perfectly explains the artificial observations is found by the inversion. In this case, the final source model does not match the ground truth exactly. While the moment tensor and source time are close to the ground truth, the location cannot be as accurately resolved as one might expect in a synthetic noise-free inversion. This demonstrates that the null-space of the problem is significant.

When noise is added to the dataset of event B, the arrival of body waves is completely masked by noise (see Fig. 3b). The updating scheme initially moves the source through model space in a manner similar to the noise-free case, which is visible in the path of the horizontal location models when comparing Figs 9(c) to 10(c). Although the location and source time are further from the ground truth than in the starting model, the misfit reduced by 96%, where the recovery of the correct source mechanism is the largest contributor.

In addition to the synthetic tomography discussed in the main body of the manuscript, we show waveform comparison of the inversion in Fig. 11. While we selected to show one event for the DAS inversions, we show the entire data set for the IFOS inversion. In the noise-free examples, the inversion finds models that almost perfectly replicate the data. It is notable that the noise level in the inversion including noise on DAS masks a lot of information about the subsurface structures in the wavefield. However, many of the target anomalies can be recognized in the final tomographic image. This can potentially be attributed to the massive amount of channels along the fibre that partly overcomes the coherent noise.

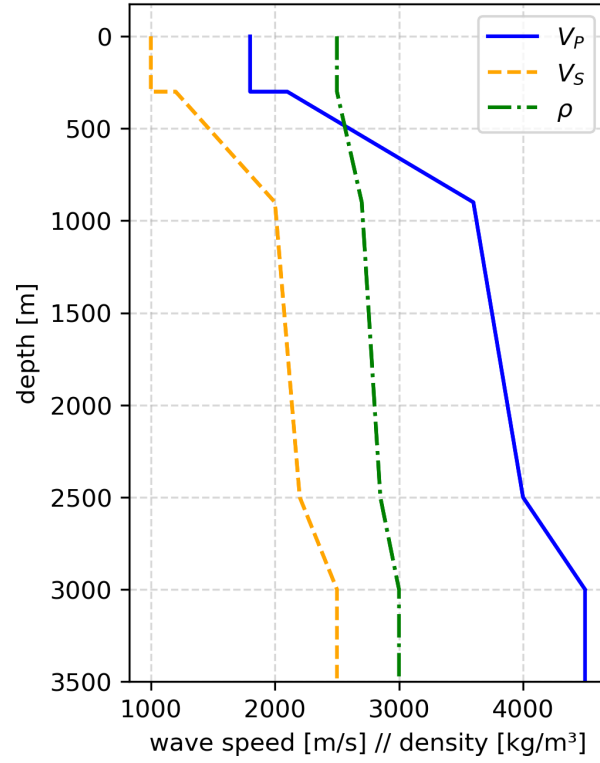


Figure 8: The 1-D background model of the domain in the synthetic inversions. For the tomographic examples, this layering is assumed to be known. The checkerboard anomalies in the subsurface ground truth are defined relative to this background model.

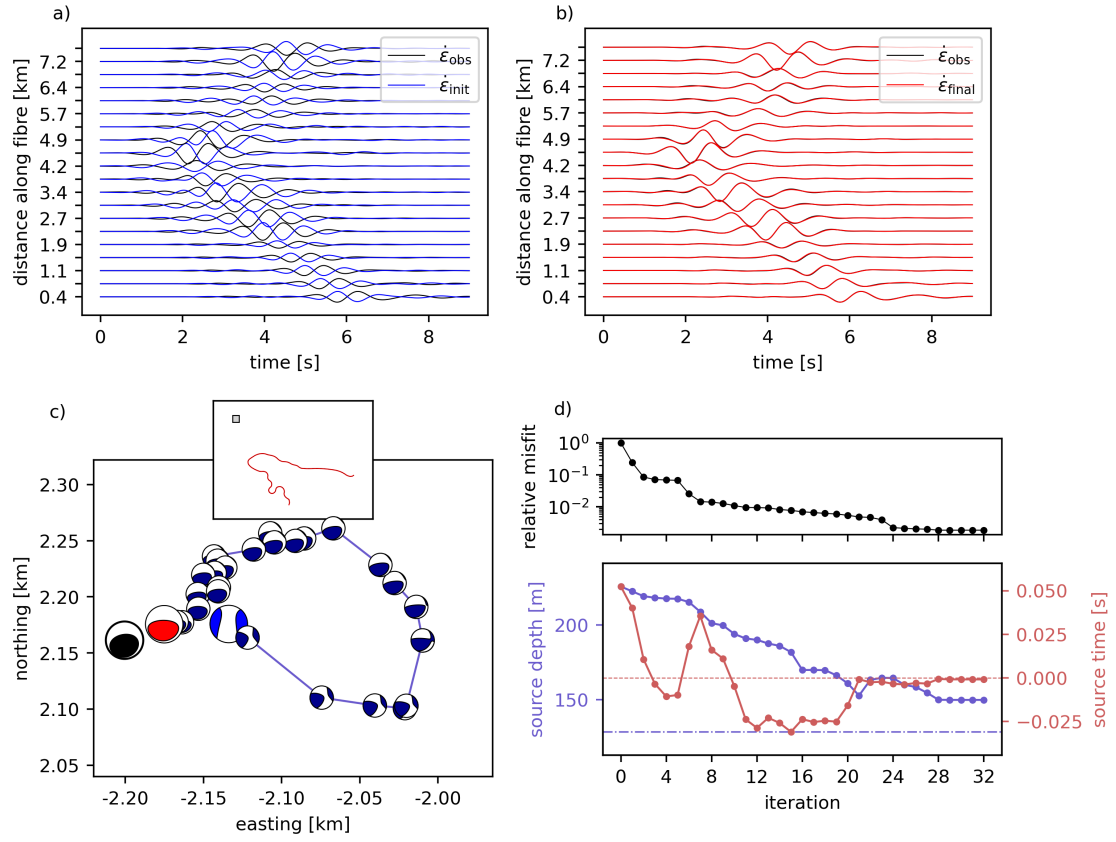


Figure 9: Noise-free inversion for DAS data of event B. For brevity, details on how to interpret the figure are omitted here and provided in the caption of Fig. 4.

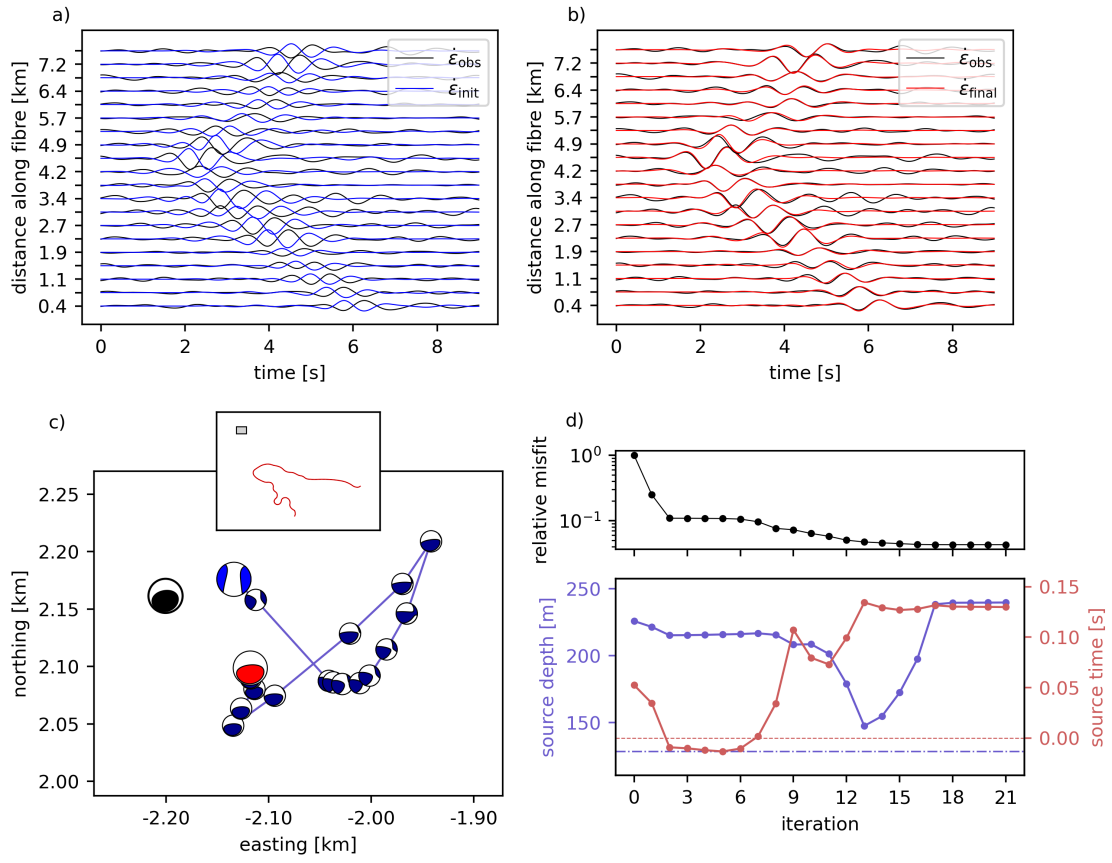


Figure 10: Source inversion for event B with noise. For brevity, details on how to interpret the figure are omitted here and provided in the caption of Fig. 4.

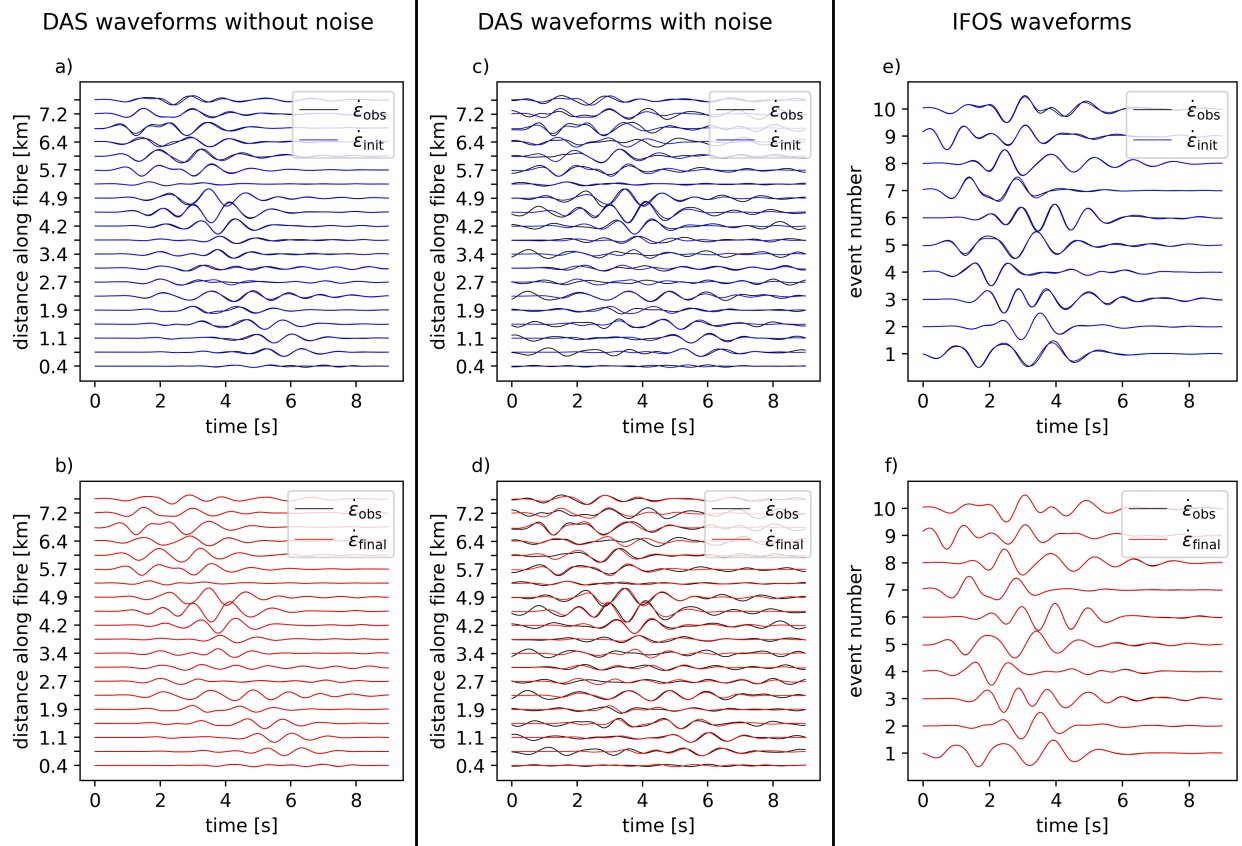


Figure 11: The comparison between modelled and observed waveforms in the tomographies is presented. Each column represents a separate inversion. In all panels, black lines represent the artificial observations, while red and blue lines correspond to the starting and final models, respectively. The structural models producing the waveforms are shown in Fig. 7. a) Comparison of noise-free observed data for one of the ten events with waveforms from the initial model. b) Comparison of noise-free observed data with waveforms from the final inverted model. c) Same as (a), but using noisy data. d) Final inverted waveforms obtained from the model using noisy artificial observations. e) Waveforms from all 10 events used in the IFOS inversion. f) Final inverted IFOS traces compared to the observed data.